ZnAl layered double hydroxide based catalysts (with Cu, Mn, Ti) used as noble metal-free three-way catalysts

Tim Van Everbroeck*[1], Jianxiong Wu[3], Daniel Arenas-Esteban[4], Radu-George Ciocarlan[1], Myrjam Mertens[2], Sara Bals[4], Christophe Dujardin[3], Pascal Granger[3], Elena M. Seftel[2], Pegie Cool[1]

[1] *Laboratory of Adsorption and Catalysis, University of Antwerp, Universiteitsplein 1, 2610 Wilrijk, Belgium.*

[2] *VITO Flemish Institute for Technological Research, Boerentang 200, 2400 Mol, Belgium*

[3] *Univ. Lille, CNRS, Centrale Lille, Univ. Artois, UMR 8181 - UCCS - Unité de Catalyse et Chimie du solide, F-59000 Lille, France*

[4] *Electron Microscopy for Materials Research (EMAT) and NANOlab Centre of Excellence, University of Antwerp, Groenenborgerlaan 171, 2020, Antwerp, Belgium*

corresponding author: tim.vaneverbroeck@uantwerpen.be

Abstract

This research presents a novel approach for developing noble metal-free three-way catalysts by using ZnAl layered double hydroxide (LDH) co-precipitated with Mn and Ti. Cu was added as the catalytically active metal. Two methods were explored, namely the addition of Cu during the co-precipitation step and a post-synthesis method using the LDH memory effect. In case the starting material had LDH characteristics high amounts of CuO were adsorbed on the support and high dispersion degrees of CuO were obtained. A four-cycle three-way catalysis test was used for evaluation. The smaller CuO particle size resulted in better performance for oxidation reactions. The addition of Mn had a positive effect on the general performance of the catalysts, while the presence of Ti mainly improved the NO conversion.

26   The developed materials showed good stability in consecutive catalytic testing cycles and even

27   show some NO conversion under stoichiometric conditions. The developed CuO-based ZnAl

28   layered double hydroxide-based materials are very promising catalysts for Three-way

29   catalysis, allowing to reduce the precious metal content compared to the classical catalysts

30   composition.

Keywords

32   Layered Double Hydroxides, memory effect, three-way catalysts, copper oxide, NO reduction,

33   CO oxidation

Highlights

35   • High loadings of well-dispersed CuO nanoparticles on layered double hydroxide (LDH)

36   • Superior catalytic performance due to well-dispersed CuO nanoparticles

37   • Amorphous aluminium oxide in the LDH material works as support dispersing CuO

38   • Increased performance with Mn addition and NO conversion with Ti addition

Introduction

40   While the technology for the production of alternatively powered vehicles has greatly

41   advanced in the past few years and the sales of diesel cars continues to fall, only 10.5 % of the

42   passenger cars registered in 2020 in the European Union relied only on electricity (European

43   Automobile Manufacturers Association, 2021). Petrol cars are equipped with a three-way

44   catalytic converter whose function is to remove CO, NO_x and hydrocarbons. The key

45   components of current three-way converters are the precious metals Pt, Pd, and Rh (Kašpar

46   et al., 2003; Kumar et al., 2017). These materials are however considered as critical raw

47   materials (CRM) because of their great economic importance, while their supply is at risk. This

48   means that their use in new technologies must be limited as much as possible (European

49   Commission, 2018). This also causes a revived interest in the use of alternative materials to

50   replace the CRMs.

51   Although having a reaction rate of about 50 times lower than Pd for CO (Kummer, 1980), CuO

52   is the preferred catalyst to focus on as it is not a CRM (European Commission, 2018). While

53   lower reaction rates could be compensated by using larger amounts of CuO, a good dispersion

54   is essential for the catalytic activity of CuO, which is challenging to achieve with larger amounts

55   on a given surface area (Bennici et al., 2004). At the same time, large amounts of CuO can

56   agglomerate easier when exposed to the high temperatures of the exhaust gas. In order to

57   avoid this, it is important to design a catalyst with a high surface area, while having highly

58   dispersed CuO deposited on the surface of the support. Another way of increasing or changing

59   the catalytic properties of a material is by the addition of a co-catalyst material. Specific metal

60   oxides can work together in a synergetic system, leading to a better performance than the

61   sum of the separate materials (Cavani et al., 1991; Weng and Delmon, 1992; Liu et al., 2019).

62   These mixtures of metal oxides (MO) will be exposed for a long time at high temperatures,

63   under different gas mixtures, and the formation of mixed metal oxides (MMO), such as spinels

64   and perovskites, is likely to occur. This can directly influence the performance of the catalyst

65   (Cousin and Ross, 1990).

66   In this work, layered double hydroxide (LDH), with different compositions, are synthesized and

67   used as precursors to further tune three-way catalyst compositions of MMOs. MMOs derived

68   from LDH are particularly interesting in catalytic applications due to their large surface area,

69   homogeneous distribution of the different components and basic character (Cavani et al.,

70   1991; Gennequin et al., 2010; Kowalik et al., 2013; Mrad et al., 2015). The LDH structure

71 consists of positively charged hydroxide layers, resulting from the mixture of divalent (such as

72 Mg^{II} or Zn^{II}) and trivalent (such as Al^{III}) or tetravalent atoms (such as Ti^{IV}) (Saber and Tagaya,

73 2003, 2008; E. M. Seftel et al., 2008; Li et al., 2017) with interstitial layers of anions (such as

74 CO_3^{2-}) that compensate for the positive charge of the metal hydroxide layers (Gennequin et

75 al., 2010). Furthermore, water molecules are also located in the interstitial layers (Cavani et

76 al., 1991). One of the most interesting properties of the LDH is that after calcination, the

77 resulted MMO-type material is able to reconstruct the original LDH structure as soon as the

78 materials are brought into contact with water and an anion source. The phenomenon is often

79 referred to as "the memory effect" (Cavani et al., 1991; Marchi and Apesteguía, 1998; Erickson

80 et al., 2005; Carja et al., 2010; Gennequin et al., 2010; Kowalik et al., 2013).

81 Cu(O) was used as the main active material and was either inserted in the material during the

82 initial LDH synthesis via co-precipitation or afterwards in an impregnation step by making use

83 of the "memory effect" property of LDH.

84 While the most common LDH consist of Mg and Al (Cavani et al., 1991), this research is based

85 on Zn and Al LDH in a 2:1 ratio. Here, Zn was chosen mainly for its structural role in the LDH

86 synthesis as well as its beneficial synergistic effect for CO oxidation when used together with

87 Cu and Ti (Saber and Zaki, 2014). Zn was partially substituted by Cu in a molar ratio of 1:1, as

88 this is the maximal amount of Cu that could be isomorphously substituted within the hydroxyl

89 layers of LDH. Promising research results for CO oxidation (Saber and Zaki, 2014) and NO

90 reduction (Yuan et al., 2013, 2014; Chen et al., 2014) were reported by using LDH based

91 catalysts featuring Ti. Therefore, several compositions of LDH containing Ti were further

92 prepared by the isomorphous substitution of trivalent Al^{III} atoms with tetravalent Ti^{IV} atoms

93 in order to improve the performances of the three-way MMO catalysts. Furthermore,

94 different formulations with Mn were synthesized, based on the promising research towards

95 NO$_x$ abatement of the Mn containing LDH (Obalová et al., 2007, 2009; Li et al., 2010, 2012; LI

96 et al., 2014; Pacultová et al., 2016).

97 The aim of this work is two-fold. Firstly, to show how LDH can be used as a basis for the

98 development of Cu-based three-way catalysts and that the reconstructive properties of LDH

99 can be utilized to further optimise CuO nanoparticles on the surface of the material as

100 opposed to the traditional co-precipitation. Secondly, to assess how different metals (Mn, Zn,

101 Al, Ti) influence the catalytic performance of CuO by interacting with it or by forming mixed

102 metal oxides.

Experimental
103

Catalyst preparation
104

105 Two synthesis strategies were explored for the preparation of copper-containing three-way

106 catalysts, e. g. direct co-precipitation at constant pH and reconstruction route by taking

107 advantage of the memory effect property of the LDH, respectively. The commercial

108 benchmark reference catalysts (0.5% Pd/CeZrO$_2$ and "TWC", a grounded commercial three-

109 way catalyst) have been supplied by Johnson Matthey, UK.

a) Co-precipitation method
110

111 The initial materials were synthesized by a common co-precipitation method for LDH, at fixed

112 pH. In a typical synthesis, 120 mL of a solution of the mixed metal salts was prepared by

113 dissolving the metal salts listed in the supplementary information in the appropriate amount

114 of water for a total concentration of 0.5 M. The molar ratios of the metals were according to

115 **¡Error! No se encuentra el origen de la referencia.**. The resulting mixed metals solution was

116   mixed with 40 mL of a 1 M Na_2CO_3 solution and was added dropwise and simultaneously with

117   a 2 M NaOH solution to a beaker while stirring. The flow of the two solutions was regulated

118   as such to maintain the pH value at 7.5. The obtained precipitate was aged under stirring for

119   24 h at room temperature. The obtained precipitate was collected by vacuum filtration,

120   washed thoroughly with water and dried overnight in an oven at 80°C(E. M. Seftel et al., 2008;

121   E. Seftel et al., 2008).

122   For simplicity reasons, the synthesized materials are labelled based on the elements in their

123   composition. The names of the samples and the ratios between the elements are displayed in

124   Table 1.

Sample name	Elements	Atomic ratio
ZA	Zn, Al	2:1
ZCA	Zn, Cu, Al	1:1:1
ZAT	Zn, Al, Ti	4:1:1
ZCAT	Zn, Cu, Al, Ti	2:2:1:1
MZAT	Mn, Zn, Al, Ti	2:2:1:1
MCAT	Mn, Cu, Al, Ti	2:2:1:1
MA	Mn, Al	2:1
MT	Mn, Ti	2:1

125   *Table 1: Composition details of the catalysts prepared via the co-precipitation method.*

126   b) Reconstruction method

127   By following the same procedure described above, copper-free LDH were also prepared and

128   further used to explore the second synthesis strategy based on the memory effect.

129   These materials were calcined at 400°C for 4 h (ramping speed of 1°C/min), followed by a slow

130   cooling down to room temperature. 1 g of these MMOs were suspended into 250 mL of 0.1

131   M copper acetate solution under stirring for 30 minutes to allow the reconstruction of the

132   initial layered structure and intercalate the copper acetate anions. Finally, the solid fraction

133   was separated by centrifugation, washed thoroughly with water and dried overnight in an

134   oven at 80°C (Carja et al., 2013).

135   The materials after calcination are additionally labelled with the temperature details (for

136   example "-400"). The materials that were impregnated with Cu according to the

137   reconstruction method are indicated with "C/" before their name.

138   Finally, all the copper-loaded materials, as prepared by the two strategies as described above,

139   were calcined at 600°C for 4 h (ramping speed of 1°C/min) before their use in the catalytic

140   experiments.

Physicochemical characterisation

142   The materials were characterized by X-ray powder diffraction (XRD) using an X-ray

143   diffractometer (PANalytical X'Pert PRO MPD) equipped with CuKα radiation (λ = 0.15406 nm).

144   The analysis was performed from $2\theta = 5 - 70°$ with a scanning speed of 0.04°/4s. The average

145   crystallite size was estimated using the Scherrer equation, which is explained in the

146   supplementary information.

147   N_2-physisorption was carried out at -196°C on a Quantachrome Quadrasorb SI automated gas

148   adsorption system. Prior to the measurements, the samples were outgassed at 60°C for 16 h

149   except for the materials calcined at 400 or 600°C. These were outgassed at 200°C for 16 h. The

150   specific surface area was calculated using the Brunauer-Emmet-Teller (BET) equation. The

151 Barret-Joyner-Halenda (BJH) method was applied to estimate the pore size distribution. The

152 total pore volume was determined at P/P_0= 0.95.

153 SEM-EDX was used to determine the surface composition, using a FEG-ESEM-EDX, FEI Quanta

154 250 by scanning the whole field instead of discrete points.

155 TEM characterization of CuO nanoparticles was performed by high-angle annular dark field

156 scanning transmission electron microscopy (HAADF-STEM) and energy dispersive X-ray

157 spectroscopy (EDS) using an aberration-corrected cubed FEI Titan microscope equipped with

158 a Super X EDS detector operating at 300 kV.

Catalytic activity measurements

160 The catalytic tests were performed in a quartz fixed bed reactor. In a typical experiment, 0.200

161 g of the powder catalyst (100 - 200 µm) was mixed with 0.200 g silicon carbide to avoid

162 limitations related to mass and heat transfer phenomena. The catalytic performance was

163 evaluated from the conversions of the different gases in a multi-cycle temperature-

164 programmed experiment. The course of the temperature as a function of time during the

165 experiment is illustrated in Supplementary Figure 1, in a relevant time-scale. More details can

166 be found in the supplementary information.

Results

Structural characterization and crystallinity of the catalysts

169 With X-ray diffraction (XRD) the crystal structures of the catalysts through the different steps

170 of the synthesis can be identified. Using the Scherrer equation, the average CuO crystallite

171 size is estimated from the (111) reflection at 38.7° and reported inTable 2. Porosity analysis of

172 the catalysts was performed by N_2-sorption. The isotherms along with the surface area of the

173   materials throughout the different steps of the synthesis are presented in the supplementary

174   information.

175   ***Cu loading on ZnAl-LDH***

176   The X-ray diffractograms of C/ZA and ZCA through the different steps of the synthesis are

177   presented in Figure 1. In both the materials after co-precipitation (ZA and ZCA) the typical

178   diffraction patterns for a ZnAl carbonate intercalated layered double hydroxide (LDH) (PDF 01-

179   075-2983 (Gates-Rector and Blanton, 2019)) are present. The typical (003) and (006) basal

180   reflections centred at 11.7 and 23° are associated with the stacking of the layers (Cavani et al.,

181   1991).

182   The calcination of ZA at 400°C leads to the collapse of the LDH structure and ZnO is crystallised,

183   which is observed by it's typical pattern (Zincite, PDF 00-036-1451 (Gates-Rector and Blanton,

184   2019)). After the reconstruction method, the structural reconstruction is confirmed by the

185   reappearance of the typical LDH refection planes in the XRD pattern in the forthcoming Cu-

186   containing material, C/ZA. The reflections are however shifted in comparison to the original

187   materials, especially the (003) diffraction plane. For the LDH materials, this diffraction plane

188   is used to calculate the interlayer distance in the structure, providing direct information of the

189   anions identity and orientation within the interlayer gallery. For example, in the case of ZA,

190   the interlayer distance is 0.76 nm (d_{003}) typical for the carbonate-containing LDH, while for

191   C/ZA it has increased to 1.25 nm (d_{003}) which indicates the intercalation of the acetate anions

192   during the reconstruction process in the presence of copper acetate aqueous solution (Prevot

193   et al., 2008). At the same time, for C/ZA, the reflection at 11.7° (d_{003}) occurs, which

194   corresponds to the original carbonate LDH structure.

195 The three-way catalysts are obtained after calcination at 600°C. Both cases (C/ZA-600 and

196 ZCA-600), feature the XRD patterns of CuO (tenorite, PDF 45-937) as well as of ZnO together

197 with a spinel phase. The general formula for a spinel structure is $A^{2+}B^{3+}_2O_4$ (A – tetrahedral

198 site, B – octahedral site). The atomic ratio for spinel generally is $M^{2+}:M^{3+} = 1:2$ as compared to

199 $M^{2+}:M^{3+} = 2:1$ for the LDH (Cavani et al., 1991; Zhao et al., 2017). This means that there will be

200 anyway a surplus of M^{2+} if the LDH is completely transformed into spinel, and this is confirmed

201 by the ZnO or CuO formation in the calcined materials. The spinel phase can be associated

202 with $ZnAl_2O_4$ (PDF 00-005-0669). However, after the calcination at 600°C, a limited amount of

203 copper can penetrate the spinel structure by substituting one of the elements in the

204 octahedral or tetrahedral sites. Due to the fact that Cu and Zn have similar values of ionic

205 radius, it is very difficult to make a distinction between the two atoms within the spinel phase

206 based on the XRD patterns.
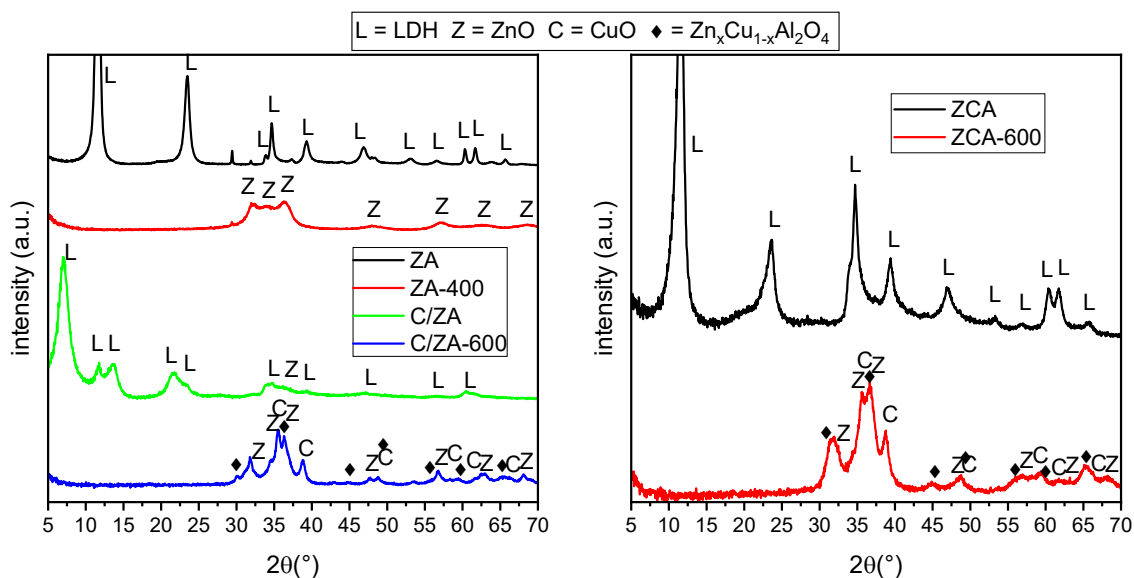
207

208 *Figure 1: X-ray diffractograms at different stages of the synthesis of C/ZA (left) and ZCA (right). ZA and ZCA are obtained by*

209 *co-precipitation. Cu-containing C/ZA is obtained by the reconstruction method. Note: the intensity of the diffractogram of ZA*

210 *has been divided by 2 in order to be displayed together with the others.*

211 ***Cu loading on ZnAlTi-LDH***

212   The diffractograms of C/ZAT and ZCAT at the different stages of the synthesis are compared

213   in Figure 2. Once more, in both ZAT and ZCAT the typical pattern of LDH after co-precipitation

214   is present. Upon calcination at 400°C, ZAT loses the LDH structure with the concomitant

215   formation of the ZnO phase. The reconstruction process in the presence of the copper acetate

216   solution leads to the intercalation of the acetate anions within the interlayer gallery of the

217   obtained LDH (C/ZAT). Further calcination at 600°C of the materials obtained by both co-

218   precipitation and reconstruction (C/ZAT-600 and ZCAT-600) are characterized by similar XRD

219   patterns with the features of CuO and ZnO combined with a $ZnAl_2O_4$ spinel phase. Due to the

220   additional presence of the Ti^{4+} cations within the LDH phase, the concomitant formation of a

221   Zn_2TiO_4 phase was further identified (PDF 01-082-1438 (Gates-Rector and Blanton, 2019)).
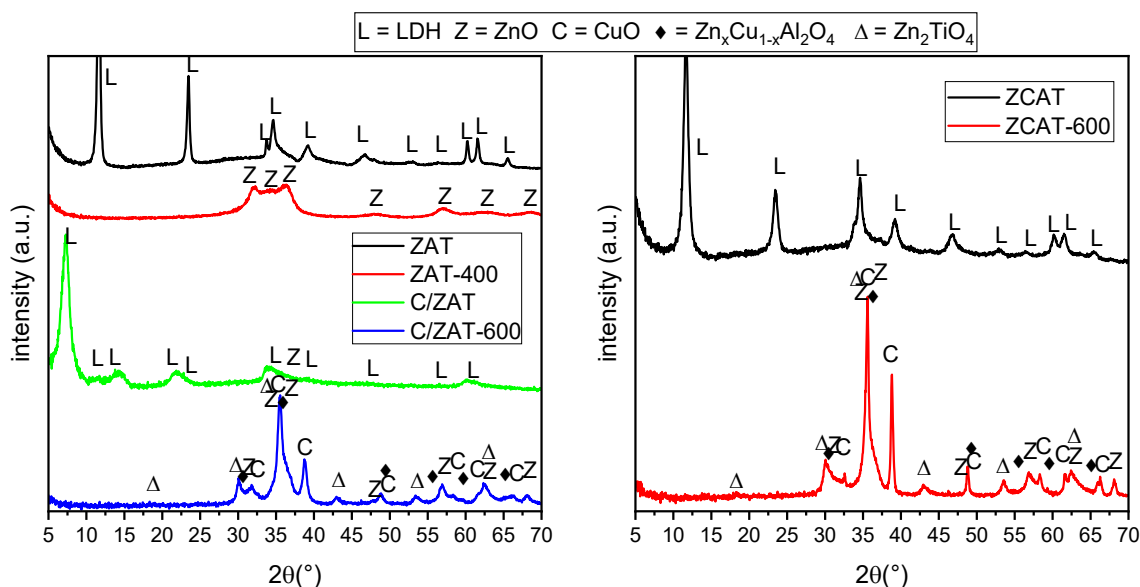

222

223   *Figure 2: X-ray diffractograms at different stages of the synthesis of C/ZAT (left) and ZCAT (right). ZAT and ZCAT are*

224   *obtained by co-precipitation, while C/ZAT contains Cu deposited by the reconstruction method.*

225   ***Cu loading on MnZnAlTi-LDH and MnCuAlTi-LDH***

226   The diffractograms of C/MZAT and MCAT in the different stages of the synthesis are displayed

227   in Figure 3. Less intense XRD diffraction lines characteristic to the LDH phase may be identified

228   for the as-prepared MZAT and MCAT material via the co-precipitation method. As such, the

229   (003) reflection characteristic to the LDH phase may be identified together with the reflections

230   of a $MnCO_3$ (Rhodochrosite, PDF 01-073-4352 (Gates-Rector and Blanton, 2019)) phase. Upon

231   calcination of the MZAT material at 400°C, the Zn_2TiO_4 phase is formed, which in the case of

232   the previously discussed ZAT material was not formed at this stage of the synthesis.

233   Furthermore, when the reconstruction procedure is applied, ZnO particles combined with a

234     $ZnMn_2O_4$ (Hetaerolite, PDF 00-024-1133) phase are formed (C/MZAT). Therefore, for this

235   initial metal composition in the LDH structure, the reconstruction process via the memory

236   effect property was not achieved, probably due to the low crystallinity of the initially obtained

237   layered structure and as well as the presence of the additional $MnCO_3$ phase. Further

238   calcination at 600°C leads to very significant differences between the obtained three-way

239   catalytic materials, e. g. the C/MZAT-600 and the MCAT-600, respectively. This can be

240   attributed to the presence of Zn. In the XRD pattern of C/MZAT-600 all the peaks may be

241   associated to structures that contain Zn, namely Zn_2TiO_4, $ZnMn_2O_4$ and ZnO, respectively,

242   while in the case of MCAT-600 these structures are not formed due to the absence of Zn ions

243   in the initial synthesis mixtures. The presence of Cu containing phase and its content is proven

244   by measuring SEM-EDX as it will be discussed in a later section. In the latter case, a spinel-like

245   phase, identified as $Cu_{1.5}Mn_{1.5}O_4$ (PDF 01-070-0262), is formed from the reaction of the high

246   amounts of Mn_2O_3 and CuO, which is in agreement with previously reported studies in

247   literature (Blasse, 1966; Vandenberghe et al., 1973, 1976; Behar et al., 2012; Biemelt et al.,

248   2016; Van Everbroeck et al., 2020).

249

L = LDH Z = ZnO M = MnCO$_3$ C = CuO Δ = Zn$_2$TiO$_4$ μ = Cu$_{1.5}$Mn$_{1.5}$O$_4$ ν = ZnMn$_2$O$_4$
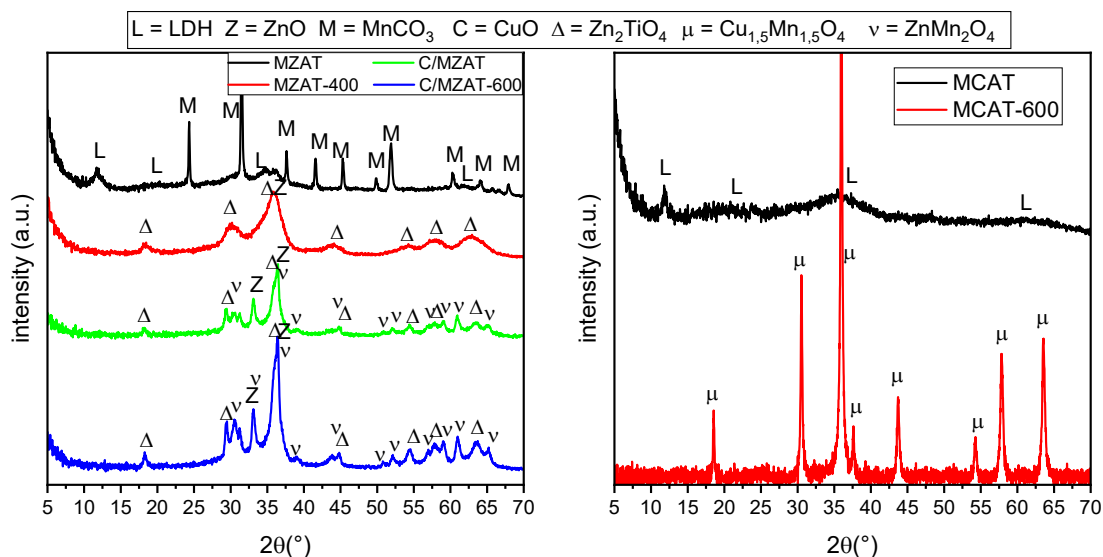
Figure 3: X-ray diffractograms at different stages of the synthesis of C/MZAT (left) and MCAT (right). MZAT and MCAT are obtained by co-precipitation. Cu-containing C/MZAT is obtained by the reconstruction method.

Cu loading on MnAl and MnTi-LDH

According to the diffractograms of C/MA and C/MT at the different stages of the synthesis, in neither of the materials the LDH structure was formed after co-precipitation (Figure 4). As a consequence, no LDH structures were formed after the reconstruction step. The only crystalline structure in the co-precipitated materials was MnCO$_3$, together with some Al(OH)$_3$ (Bayerite, PDF 01-077-0250 (Gates-Rector and Blanton, 2019)) in the case of the as-synthesized MA material. Calcining at 400°C and applying the reconstruction procedure leads to very similar materials. There are still some remnants of the MnCO$_3$ phase together with MnO$_2$ (Akhtenskite, PDF 01-089-5171 (Gates-Rector and Blanton, 2019)). Finally, the heat treatment of the catalysts at 600°C leads to the transformation of the MnO$_2$ phase into a mixture of Mn$_2$O$_3$ (Bixbyite PDF 31-825) and Mn$_3$O$_4$ (PDF 86-2337), while there is no indication of a spinel phase formation, such as Cu$_{1.5}$Mn$_{1.5}$O$_4$ in the XRD patterns. A TiO$_2$ rutile phase (PDF 00-021-1276) can additionally be found in MT-600.

13

M = MnCO₃ A = Al(OH)₃ α = MnO₂ β = Mn₂O₃ γ = Mn₃O₄ R = TiO₂ (rutile)
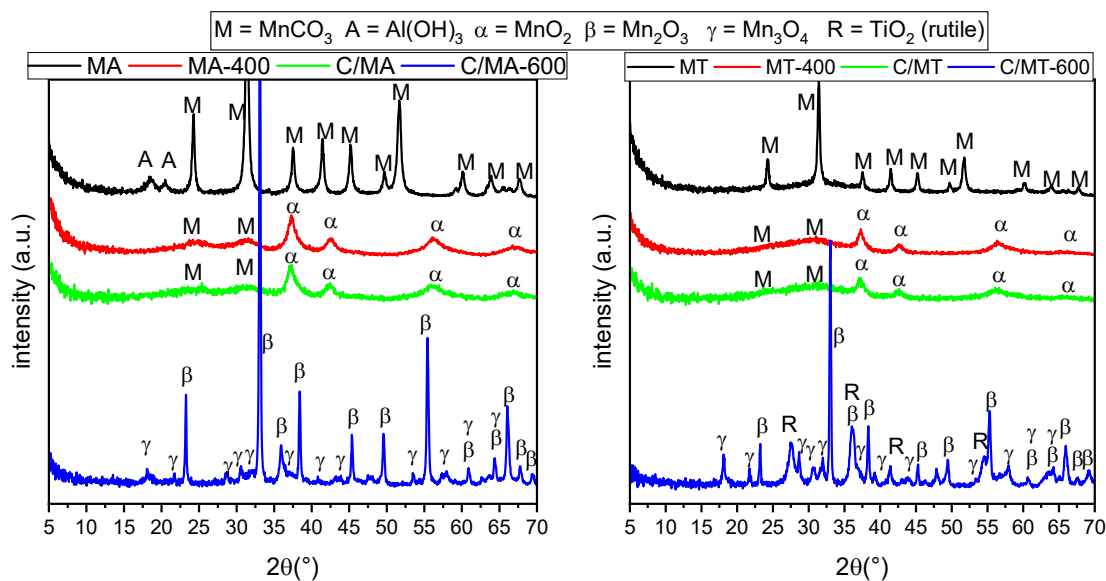
Figure 4: X-ray diffractograms at different stages of the synthesis of C/MA (left) and C/MT (right). MA and MT are obtained by co-precipitation and C/MA contains Cu deposited by the reconstruction method.

Quantification of Cu loading in the three-way catalysts

The Cu content of the final materials as determined by SEM-EDX and the average CuO crystallite size before and after the catalytic test is summarized in Table 2. The Cu content is around 35-40% for the materials that had Cu included in the first co-precipitation synthesis step (ZCA-600, ZCAT-600 and MCAT-600), but it is further increased by applying the reconstruction synthesis route on the calcined LDH materials C/ZA-600 and C/ZAT-600. Lower copper loadings are achieved in the case of the parent materials that did not display the characteristics of a well-layered structure after the co-precipitation process, such as C/MZAT, C/MA and C/MT. The precursors used in their preparation did not present only an LDH-type structure but a combination with other crystalline phases or sometimes a more amorphous character. It should be noted that, for all the prepared catalysts, the exact same concentration of copper acetate solution is used. Large variations in the crystallites sizes of the CuO nanoparticles, e. g. 7 nm and 26 nm, respectively occur in ZCA-600 and ZCAT-600 prepared via the co-precipitation method. On the other hand, by following the reconstruction method,

283 similar sizes of the CuO crystallites of ±10 nm, are achieved, namely for the C/ZA-600 and

284 C/ZAT-600 three-way catalysts. After the catalytic test, the CuO crystallite sizes increase for

285 most of the materials, except for ZCAT-600. While 18 nm CuO crystals are formed for MCAT-

286 600 after the test, no CuO crystals are XRD discernible in any of the other Mn-containing

287 materials, indicating that these CuO crystallites have sizes that are probably below 3 nm.

288

Sample	Cu content (wt%)	CuO crystallite size (before cat. test) (nm)	CuO crystallite size (after cat. test) (nm)
ZCA-600	37	7	14
C/ZA-600	62	11	15
ZCAT-600	35	26	21
C/ZAT-600	56	10	15
MCAT-600	41	-	18
C/MZAT-600	10	-	-
C/MA-600	11	-	-
C/MT-600	11	-	-

289 *Table 2: Cu content and estimated CuO crystallite size of the final materials (before and after the catalytic test). Copper*
290 *content determined by SEM-EDX. CuO size calculated with the Scherrer equation.*

291 Energy-dispersive X-ray spectroscopy (STEM-EDS) maps were acquired from different areas

292 on samples ZCAT-600, C/ZAT-600 and C/MA-600 to further investigate the size of the CuO

293 nanoparticles and their distribution. Figure 5 shows HAADF-STEM images and their respective

294 elements composition, obtained on representative areas for each sample. Whereas for ZCAT-

295 600 and C/ZAT-600 samples it is easy to find isolated zones that clearly indicate the presence

296   of Cu (Figure 5b, d), such areas are absent in the C/MA-600 sample due to a high degree of

297   agglomeration between particles. Even so, some isolated CuO nanoparticles are marked in

298   Figure 5f with red circles. CuO nanoparticles adopt a rectangular shape in all three cases, with

299   an average nanoparticle size, determined by STEM-EDS, of 35 ± 17 nm, 15 ± 11 nm and 20 ± 8

300   nm for the ZCAT-600, C/ZAT-600 and C/MA-600 composites respectively (seeSupplementary

301   figure 8). These values do not exactly match the sample size obtained in bulk, which can be

302   understood since TEM is a very local technique. Nevertheless, the particle size trend is

303   confirmed, with bigger particles for the ZCAT-600 sample in comparison to the C/ZAT-600. On

304   the other hand, for the C/MA-600 sample, CuO nanoparticles are observed in small quantities,

305   which explains why they are not detected by XRD.

306
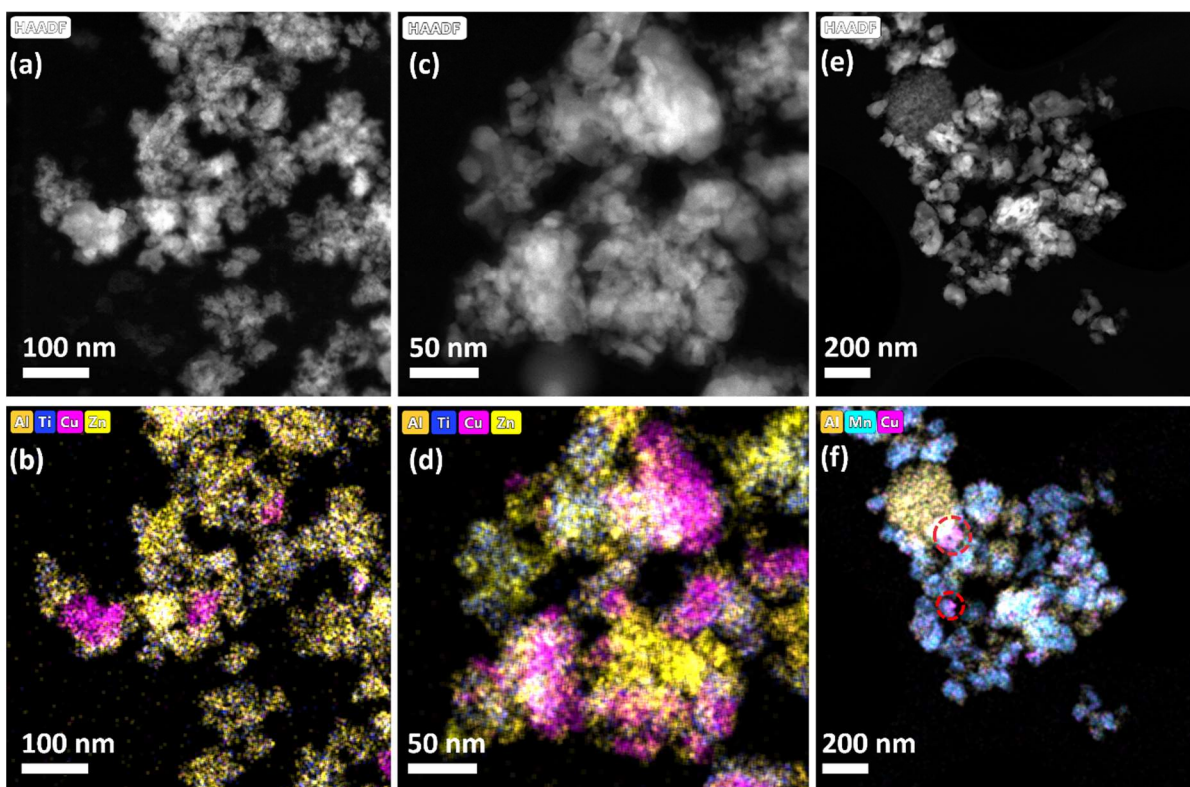
307 *Figure 5: HAADF-STEM images and their respective EDS elemental distribution for (a, b) ZCAT-600, (c, d) C/ZAT-600 and (e, f)*
308 *C/MA-600 composites. For the EDS maps, Al is marked in brown, Ti in dark blue, Cu in pink, Zn in yellow and Mn in light blue.*

Catalytic activity testing

As described in the experimental section, the catalytic test consists of four heating and cooling cycles in three different gas compositions, after an initial pre-treatment cycle. The conversions of NO, CO, propene (C_3H_6) and propane (C_3H_8) as a function of temperature during heating in the different cycles are displayed in Figure 6 and Supplementary Figure 9 to 11. The temperatures at which 50% conversion (Light-off temperature, T_{50}) is reached and, in case of the NO conversion, the maximal conversion and temperature at which this conversion is reached can be found in tables in the supplementary info. Light-off temperatures at 50% conversion are typically used in temperature-programmed experiments to indicate the onset temperature of significant catalytic activity (Biasin et al., 2019).

In the first stoichiometric cycle (Figure 6Figure 6), NO conversion generally does not reach over 10%. All the NO conversions display local maxima, only for C/MA-600 the NO conversion keeps rising until the end of the measurements. The maximum NO conversion is notably higher for C/ZAT-600, C/MZAT-600, C/MA-600 and C/MT-600. The temperature of 50% CO conversion is the lowest for C/MA-600, C/MT-600 and C/MZAT-600, while ZCAT-600 differentiates the most from the others for a much higher T_{50}. On the other hand, the propene conversion curves are much more diverse. While C/MZAT-600 and C/ZAT-600 have a T_{50} around 330 and 350°C, C/MT-600 and MCAT-600 only reach this above 520°C. Propane conversion generally only starts above 500°C. The only exception is in the case of C/MA-600, which reaches even 50% under 500°C.

330
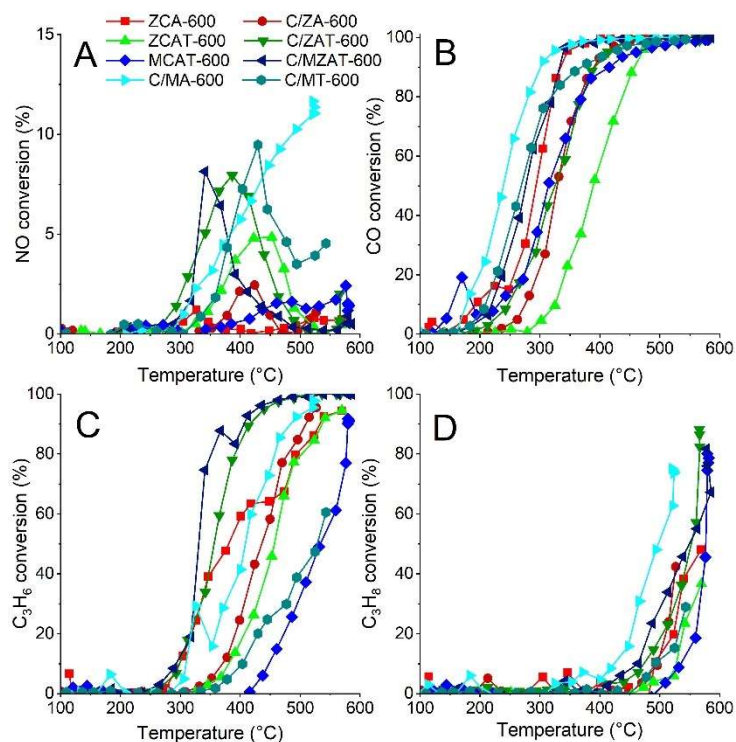
Figure 6: Temperature programmed conversion curves under stoichiometric conditions, first cycle, A: NO conversion, B: CO

conversion, C: propene conversion, D: propane conversion.

Discussion

Layered double hydroxides have been successfully formed even if the Zn^{II} atoms were partially

substituted by Cu^{II} or Al^{III} atoms are partially substituted by Ti^{IV}, in both cases for a substitution

degree of 50 mol%. The incorporation of large quantities of Mn atoms in the LDH structure is

however not as straightforward, due of the fact that Mn atoms lead to octahedral distortions

(similarly to Cu atoms) as a result of the Jahn-Teller effect (Cavani et al., 1991; Fridrichová et

al., 2017). In the cases of MCAT and MZAT, there is still evidence of the LDH structure, but the

experiments prove that Cu or Zn are essential to form the LDH structure with Al (and Ti).

Aisawa *et al.* reported that when CO_3^{2-} is used as the anion source for the synthesis of Mn-Al

LDH, the LDH could still be formed but $MnCO_3$ could also be formed, which is indeed the case

here (Aisawa et al., 2002).

18

345 While no indications of the LDH-like structure after calcination at 400°C in the XRD results, the

346 LDH structure is reformed after suspension in an aqueous copper acetate solution, even after

347 a long time at ambient conditions. The experiments prove that it is essential for the LDH

348 structure to have a high crystallinity for the starting material in order to exhibit these

349 reconstructive properties. In the case of MZAT, the low intensity of the LDH characteristic XRD

350 reflections as well as the presence of the $MnCO_3$ segregated phase indicate that the material

351 is very unlikely to reconstruct. Accordingly, the materials that do not have the LDH structure

352 before calcination will also not form LDH-like structures when mixed with the copper acetate

353 solution. Besides the characteristic (003) plane of acetate intercalated LDH, the XRD patterns

354 of C/ZA show (Figure 1) another reflection maximum at 11.7°, characteristic to the original

355 carbonate LDH. This can be related to the presence of CO_2 in the air or CO_2 in the aqueous

356 acetate solution (Stanimirova and Balek, 2008).

357 The current experiments suggest that the reconstructed LDH materials are able to take-up

358 large amounts of copper between their layers. After all the synthesis steps, the materials with

359 LDH structure retain up to 6 times more copper (around 60 wt%) than those without LDH

360 structure (around 10 wt%) (Table 2). The thermal decomposition of LDH generally consists out

361 of two phases. At around 200°C the interstitial water is lost, while between 300 and 450°C

362 generally the hydroxyl groups and carbonate are removed (Reichle et al., 1986). From XRD, it

363 is observed that at 400°C some oxides such as ZnO are already crystallised, but the mixed

364 oxides, such as spinels are not yet detectible in the XRD patterns. This means that the mixed

365 oxides are still amorphous, so the lamellar microstructure of LDH is still there, albeit not as

366 crystalline to be discernible with XRD. These LDOs (layered double oxides) obtained by

367 calcination at mild temperatures are known to be very effective to intercalate anions via the

368 reconstruction based on the memory effect mechanism (Seftel et al., 2018). Although it seems

369   counterintuitive, LDH are also able to adsorb metal cations from a solution. This can occur

370   through multiple mechanisms such as precipitation, surface complexation, isomorphic

371   substitution or chelation (Liang et al., 2013). It can be stated that the intercalation of the

372   anionic species occurs concomitantly with the rehydroxylation of the brucite-like layers. As

373   such, the presence of the hydroxyl groups on the surface of the LDH enables all these

374   mechanisms, explaining why the materials that did not exhibit LDH characteristics in this study

375   did not take up high amounts of Cu^{II}. To determine the exact mechanism that takes place in

376   the experiments more research is needed, which is beyond the scope of the current study.

377   The estimated CuO crystallite size is much larger for ZCAT-600 in comparison to the other

378   catalysts, while the Cu content is much lower in ZCAT-600 than in C/ZAT-600 and C/ZA-600

379   (Table 2). This seems to suggest that the reconstruction method leads to much better

380   dispersed CuO in the final material, than by adding copper during the LDH synthesis via the

381   direct co-precipitation route. On the other hand, ZCA-600 contains about the same amount of

382   copper as ZCAT-600, but the CuO size is considerably smaller. For the calcined catalysts, Cu is

383   also likely to be found in the mixed oxide phases (such as $ZnAl_2O_4$ and Zn_2TiO_4) explaining the

384   difference between ZCAT-600 and ZCA-600; Cu is likely to form $CuAl_2O_4$ or together with zinc

385   in a $Zn_xCu_{1-x}Al_2O_4$ spinel after calcination at high temperature (Friedman et al., 1978; Mista et

386   al., 2003; Patel et al., 2015, 2017). This is certainly the reason why no CuO phase could be

387   detected in MCAT-600 by XRD analysis. When mixed together, the solid-state reaction

388   between the CuO and Mn_2O_3 is very likely to form a spinel phase even at temperatures lower

389   than 600°C (Vandenberghe et al., 1973; Van Everbroeck et al., 2020). For C/MA-600 and C/MT-

390   600, the measured copper content is low, resulting in CuO nanoparticles not being detectable

391   by XRD analysis (Figure 4). However, after the catalytic tests, the crystallite size of CuO has

392   increased in some of the catalysts due to the sintering process. Interestingly, in the case of

393 ZCAT-600, there is even a slight decrease of CuO crystallite size; this could be possibly

394 correlated to the diffusion of copper ions into the mixed oxides. The most notable change of

395 the CuO crystallites size is occurring within the MCAT-600 catalyst. In this case, before the

396 catalytic test, no CuO could be detected in XRD, while after the catalytic test, which can be

397 found in the supplementary information, the XRD analysis indicates the presence of CuO

398 crystals with sizes of around 18 nm. This may be due to the transformation of $Cu_{1.5}Mn_{1.5}O_4$

399 phase into a $CuMn_2O_4$ type phase as it was indicated evidenced by XRD analysis (Supplementary

400 figure 26). Part of the Cu^{2+} segregates from the structure and agglomerates as CuO.

401 The profiles of the CO conversion as a function of temperature under all the different

402 conditions indicate that the ZCAT-600, which has the largest CuO crystallite size, always

403 achieves the highest T_{50}. C/ZA-600 and C/ZAT-600 perform very similar which can be assigned

404 to the fact that these contain similar loadings of CuO with sizes in the same range. Only in the

405 lean and second stoichiometric cycle, C/ZA-600 shows a relatively higher T_{50} than C/ZAT-600.

406 At the same time, ZCA-600 reaches a lower T_{50} in the first stoichiometric cycle than C/ZAT-

407 600, again related to the smaller CuO size. However, in the second stoichiometric cycle, it

408 performs very comparable to C/ZAT-600, likely due to the growth of CuO crystallites. CO

409 oxidation at lower temperatures due to smaller or more disperse CuO particles has been

410 reported before. Higher CuO loading is also advantageous for CO conversion but only if good

411 dispersion can be assured(Luo et al., 2005; Xin et al., 2016). By using the LDH memory effect

412 both a high loading and good dispersion was ensured in C/ZAT-600 compared to ZCAT-600.

413 The Mn containing materials are generally superior for the CO conversion than those without.

414 C/MA-600 has in every case the lowest T_{50}, while MCAT-600 has most of the times the highest

415 T_{50}. Again, MCAT-600 has a much higher copper content and after the test it aggregates into

416   large CuO crystallites, explaining the higher T_{50}. The remarkable performance of the Cu-Mn

417   compounds for CO oxidation is known since the first World War (1920), when mixtures of CuO

418   and MnO_2 , known as hopcalite, were studied to be used in gas masks to prevent CO poisoning

419   (Lamb et al., 1920; Almquist and Bray, 1923; Bliss, 1955). The difference between the materials

420   used for gas masks and the materials in this application (three-way catalysis) is that the gas

421   masks need to operate around room temperature, while for three-way catalysis it operates

422   for long periods at high temperatures. In the case of three-way catalysis, the materials are

423   already calcined at 600°C, so the crystallisation of the compounds explains why they are

424   unable to convert CO at room temperature. For MCAT-600, the copper manganite structure

425   is more crystalline than the other compounds, which can also explain the higher T_{50} for CO. A

426   possible reason for the best performance of C/MA-600 for CO conversion is related to the

427   amorphous alumina present, which helps disperse the Cu and Mn mixtures over the entire

428   material, inhibiting their agglomeration and further crystallization. Furthermore, the higher

429   surface area of C/MA-600 as compared to C/MT-600 and C/MZAT-600 also contributes to

430   better dispersion. Moreover, the propene/propane conversion profiles and the benchmarking

431   of the catalyst are discussed in detail in the Supplementary Information. A further discussion

432   on the mechanisms that take place on CuO and copper manganite can be found in the

433   literature (Cocke and Vepřek, 1986; Vepřek et al., 1986; Buciuman et al., 1999; Van Everbroeck

434   et al., 2020).

435   The formation of N_2O and NH_3 can occur from NO reduction, as reaction intermediates (Jobson

436   et al., 1994; Okamoto and Gotoh, 1997; Okamoto et al., 1997; Granger et al., 2004; Nevalainen

437   et al., 2018). In the current experiments, no N_2O is detected at low temperatures in

438   stoichiometric and lean conditions, while in rich conditions, small quantities (< 20 ppm) of N_2O

439   are sometimes detected above 400°C. Overall, the selectivity towards N_2O is very low. A

440   further discussion is on the NO conversion and selectivity is presented in the Supplementary

441   Information. Furthermore, corresponding stoichiometric, lean and rich conditions results as

442   well as reaction rates taking into account (i) specific surface area (Supplementary Figure 16,

443   17 and 18) and the (ii) amount of reactive sites of the catalyst (Supplementary Figure 19, 20

444   and 21) are detailed in the Supplementary Information.

445   To demonstrate the stability of the materials a structural investigation of the spent catalysts

446   is also presented in the Supplementary Information.

Conclusions

448   Layered double hydroxides with various compositions were prepared to obtain copper oxide

449   containing three-way catalysts. The Cu source was added following two different methods, (a)

450   during the LDH synthesis via co-precipitation and (b) by reconstruction of the calcined LDOs

451   material based on the unique memory effect property. Larger amounts of CuO nanoparticles

452   can be loaded on the three-way catalysts by using the reconstruction method, but a well-

453   crystallized starting LDH structure is necessary for an effective reconstruction process.

454   Catalytic testing of the obtained three-way catalysts showed that the CO and the

455   hydrocarbons, e. g. propene and propane, were generally converted at lower temperatures

456   when CuO crystallites were smaller and well-dispersed. A synergistic effect was observed

457   when Mn atoms were present in the catalysts structure. Further, it was demonstrated that a

458   better dispersion of CuO was more important than achieving high loadings of CuO

459   nanoparticles on the three-way catalysts. The presence of Al in the LDH layers creates a more

460   appropriate support material, compared to the presence of Ti in the layers, due to the fact

461   that it enabled a higher Cu dispersion and provided a higher surface area. The main drawback

462   observed in the case of Ti-containing catalysts is directly related to its crystallisation to rutile,

23

463 after long exposure to high temperatures. However, the addition of Zn prevented the

464 crystallisation of rutile by the formation of Zn_2TiO_4, which was advantageous for the propene

465 conversion process. On the other hand, the presence of Ti proved to be beneficial for the

466 conversion and the selectivity towards N_2 in the NO conversion. Highly dispersed CuO on the

467 supporting material was again one of the most important factors to reach a high catalyst

468 activity. These conclusions offer new insights in the design of LDH-based MMOs for the

469 reduction of CRMs in three-way catalytic convertors.

Acknowledgements

Bibliography

477 Aisawa, S., Hirahara, H., Uchiyama, H., Takahashi, S., Narita, E., 2002. Synthesis and Thermal

478   Decomposition of Mn–Al Layered Double Hydroxides. J. Solid State Chem. 167, 152–159.

479   https://doi.org/https://doi.org/10.1006/jssc.2002.9637

480 Almquist, J.A., Bray, W.C., 1923. The Catalytic Oxidation of Carbon Monoxide. I. Efficiency of the

481   Catalysts, Manganese Dioxide, Cupric Oxide and Mixtures of These Oxides. J. Am. Chem. Soc.

482   45, 2305–2322. https://doi.org/10.1021/ja01663a011

483 Behar, S., Gonzalez, P., Agulhon, P., Quignard, F., Świerczyński, D., 2012. New synthesis of nanosized

484   Cu–Mn spinels as efficient oxidation catalysts. Catal. Today 189, 35–41.

485   https://doi.org/10.1016/J.CATTOD.2012.04.004

486   Bennici, S., Carniti, P., Gervasini, A., 2004. Bulk and Surface Properties of Dispersed CuO Phases in

487   Relation with Activity of NOxReduction. Catal. Letters 98, 187–194.

488   https://doi.org/10.1007/s10562-004-8679-9

489   Biasin, A., Fabro, J., Michelon, N., Glisenti, A., Canu, P., 2019. Investigation of thermal effects on

490   heterogeneous exothermic reactions and their impact on kinetics studies. Chem. Eng. J.

491   https://doi.org/10.1016/j.cej.2018.10.116

492   Biemelt, T., Wegner, K., Teichert, J., Lohe, M.R., Martin, J., Grothe, J., Kaskel, S., 2016. Hopcalite

493   nanoparticle catalysts with high water vapour stability for catalytic oxidation of carbon

494   monoxide. Appl. Catal. B Environ. 184, 208–215. https://doi.org/10.1016/J.APCATB.2015.11.008

495   Blasse, G., 1966. Ferromagnetism and ferrimagnetism of oxygen spinels containing tetravalent

496   manganese. J. Phys. Chem. Solids 27, 383–389. https://doi.org/10.1016/0022-3697(66)90045-X

497   Bliss, A., 1955. Arthur Becket Lamb February 25,1880 - May 15, 1952. J. Am. Chem. Soc. 77, 5773–

498   5780. https://doi.org/10.1021/ja01627a600

499   Buciuman, F.C., Patcas, F., Hahn, T., 1999. A spillover approach to oxidation catalysis over copper and

500   manganese mixed oxides. Chem. Eng. Process. Process Intensif. 38, 563–569.

501   https://doi.org/10.1016/S0255-2701(99)00053-7

502   Carja, G., Dartu, L., Okada, K., Fortunato, E., 2013. Nanoparticles of copper oxide on layered double

503   hydroxides and the derived solid solutions as wide spectrum active nano-photocatalysts. Chem.

504   Eng. J. 222, 60–66. https://doi.org/10.1016/j.cej.2013.02.039

505   Carja, G., Kameshima, Y., Ciobanu, G., Okada, K., 2010. Oleate-LDH hybrids by the successive use of

506   the clay structural "memory effect," in: Journal of Nanoscience and Nanotechnology.

507   https://doi.org/10.1166/jnn.2010.1389

508   Cavani, F., Trifiro, F., Vaccari, A., 1991. Hydrotalcite-type anionic clays: Preparation, properties and

509   applications. Catal. Today 11, 173–301. https://doi.org/10.1016/0920-5861(91)80068-K

510 Chen, L., Si, Z., Wu, X., Weng, D., 2014. DRIFT Study of CuO–CeO2–TiO2 Mixed Oxides for NOx

511   Reduction with NH3 at Low Temperatures. ACS Appl. Mater. Interfaces 6, 8134–8145.

512   https://doi.org/10.1021/am5004969

513 Choukroun, D., Daems, N., Kenis, T., Van Everbroeck, T., Hereijgers, J., Altantzis, T., Bals, S., Cool, P.,

514   Breugelmans, T., 2020. Bifunctional Nickel–Nitrogen-Doped-Carbon-Supported Copper

515   Electrocatalyst for CO2 Reduction. J. Phys. Chem. C 124, 1369–1381.

516   https://doi.org/10.1021/acs.jpcc.9b08931

517 Clarke, T.J., Davies, T.E., Kondrat, S.A., Taylor, S.H., 2015. Mechanochemical synthesis of copper

518   manganese oxide for the ambient temperature oxidation of carbon monoxide. Appl. Catal. B

519   Environ. https://doi.org/10.1016/j.apcatb.2014.09.070

520 Cocke, D.L., Vepřek, S., 1986. First direct evidence of a solid state charge transfer redox system Cu+2

521   + Mn3+ ⇋ Cu1+ + Mn4+in copper manganese oxide. Solid State Commun. 57, 745–748.

522   https://doi.org/10.1016/0038-1098(86)90851-3

523 Cousin, P., Ross, R.A., 1990. Preparation of mixed oxides: a review. Mater. Sci. Eng. A 130, 119–125.

524   https://doi.org/10.1016/0921-5093(90)90087-J

525 Erickson, K.L., Bostrom, T.E., Frost, R.L., 2005. A study of structural memory effects in synthetic

526   hydrotalcites using environmental SEM. Mater. Lett. 59, 226–229.

527   https://doi.org/https://doi.org/10.1016/j.matlet.2004.08.035

528 European Automobile Manufacturers Association, 2021. Fuel types of new cars: electric 10.5%,

529   hybrid 11.9%, petrol 47.5% market share full-year 2020 [WWW Document]. 4/2/2021. URL

530   https://www.acea.auto/fuel-pc/fuel-types-of-new-cars-electric-10-5-hybrid-11-9-petrol-47-5-

531   market-share-full-year-2020/ (accessed 11.11.21).

532 European Commission, 2018. Report on Critical Raw Materials and the Circular Economy Part 1/3,

533   Commission staff working document. https://doi.org/10.1097/PPO.0b013e3181b9c5d5

534   Fridrichová, J., Bacik, P., Ertl, A., Wildner, M., Dekan, J., Miglierini, M., 2017. Jahn-Teller distortion of

535   Mn 3+ -occupied octahedra in red beryl from Utah indicated by optical spectroscopy. J. Mol.

536   Struct. 1152. https://doi.org/10.1016/j.molstruc.2017.09.081

537   Friedman, R.M., Freeman, J.J., Lytle, F.W., 1978. Characterization of $CuAl_2O_3$ catalysts. J. Catal. 55,

538   10–28. https://doi.org/https://doi.org/10.1016/0021-9517(78)90181-1

539   Gates-Rector, S., Blanton, T., 2019. The Powder Diffraction File: a quality materials characterization

540   database. Powder Diffr. 34, 352–360. https://doi.org/DOI: 10.1017/S0885715619000812

541   Gennequin, C., Barakat, T., Tidahy, H.L., Cousin, R., Lamonier, J.-F., Aboukaïs, A., Siffert, S., 2010. Use

542   and observation of the hydrotalcite "memory effect" for VOC oxidation. Catal. Today 157, 191–

543   197. https://doi.org/https://doi.org/10.1016/j.cattod.2010.03.012

544   Gong, J., Liu, T., Wang, X., Hu, X., Zhang, L., 2011. Efficient Removal of Heavy Metal Ions from

545   Aqueous Systems with the Assembly of Anisotropic Layered Double Hydroxide

546   Nanocrystals@Carbon Nanosphere. Environ. Sci. Technol. 45, 6181–6187.

547   https://doi.org/10.1021/es200668q

548   Granger, P., Malfoy, P., Leclercq, G., 2004. Kinetics of the $CO+N_2O$ reaction over noble metals: II.

549   Rh/Al_2O_3 and $Pt–Rh/Al_2O_3$. J. Catal. 223, 142–151.

550   https://doi.org/https://doi.org/10.1016/j.jcat.2004.01.017

551   Hargreaves, J.S.J., 2016. Some considerations related to the use of the Scherrer equation in powder

552   X-ray diffraction as applied to heterogeneous catalysts. Catal. Struct. React. 2, 33–37.

553   https://doi.org/10.1080/2055074X.2016.1252548

554   Iwamoto, M., Yahiro, H., 2003. Zeolites in the Science and Technology of Nitrogen Monoxide

555   Removal. https://doi.org/10.1201/9780203911167.ch19

556   Jahn, H.A., Teller, E., Donnan, F.G., 1937. Stability of polyatomic molecules in degenerate electronic

557   states - I—Orbital degeneracy. Proc. R. Soc. London. Ser. A - Math. Phys. Sci. 161, 220–235.

558   https://doi.org/10.1098/rspa.1937.0142

559   Jobson, E., Smedler, G., Malmberg, P., Bernler, H., Hjortsberg, O., Gottberg, I., Rosén, Å., 1994.

560   Nitrous Oxide Formation Over Three-Way Catalyst. SAE Trans. 103, 519–530.

561   Kašpar, J., Fornasiero, P., Hickey, N., 2003. Automotive catalytic converters: current status and some

562   perspectives. Catal. Today 77, 419–449. https://doi.org/https://doi.org/10.1016/S0920-

563   5861(02)00384-X

564   Kowalik, P., Konkol, M., Kondracka, M., Próchniak, W., Bicki, R., Wiercioch, P., 2013. Memory effect

565   of the CuZnAl-LDH derived catalyst precursor—In situ XRD studies. Appl. Catal. A Gen. 464–465,

566   339–347. https://doi.org/https://doi.org/10.1016/j.apcata.2013.05.048

567   Kumar, K., Kumar, N., Singh, H., 2017. Comprehensive Review of Three way Catalytic Converter 3,

568   1188–1196.

569   Kummer, J.T., 1980. Catalysts for automobile emission control. Prog. Energy Combust. Sci. 6, 177–

570   199. https://doi.org/10.1016/0360-1285(80)90006-4

571   Lamb, A.B., Bray, W.C., Frazer, J.C.W., 1920. The Removal of Carbon Monoxide from Air. J. Ind. Eng.

572   Chem. 12, 213–221. https://doi.org/10.1021/ie50123a007

573   Larsson, P.-O., Andersson, A., 1998. Complete Oxidation of CO, Ethanol, and Ethyl Acetate over

574   Copper Oxide Supported on Titania and Ceria Modified Titania. J. Catal. 179, 72–89.

575   https://doi.org/10.1006/JCAT.1998.2198

576   Larsson, P.O., Andersson, A., Wallenberg, L.R., Svensson, B., 1996. Combustion of CO and toluene;

577   characterisation of copper oxide supported on titania and activity comparisons with supported

578   cobalt, iron, and manganese oxide. J. Catal. https://doi.org/10.1006/jcat.1996.0329

579   Li, Q., Meng, M., Dai, F., Zha, Y., Xie, Y., Hu, T., Zhang, J., 2012. Multifunctional hydrotalcite-derived

580   K/MnMgAlO catalysts used for soot combustion, NOx storage and simultaneous soot–NOx

581   removal. Chem. Eng. J. 184, 106–112.

582   https://doi.org/http://dx.doi.org/10.1016/j.cej.2012.01.009

583   Li, Q., Meng, M., Xian, H., Tsubaki, N., Li, X., Xie, Y., Hu, T., Zhang, J., 2010. Hydrotalcite-Derived

584   MnxMg3−xAlO Catalysts Used for Soot Combustion, NOx Storage and Simultaneous Soot-NOx

585   Removal. Environ. Sci. Technol. 44, 4747–4752. https://doi.org/10.1021/es9033638

586   LI, Q., WANG, X., CHANG, W., CHEN, H., ZHANG, Z., 2014. Promotional effects of cerium doping and

587   NOx on the catalytic soot combustion over MnMgAlO hydrotalcite-based mixed oxides. J. Rare

588   Earths 32, 176–183. https://doi.org/https://doi.org/10.1016/S1002-0721(14)60048-X

589   Li, Y., Tang, L., Ma, X., Wang, X., Zhou, W., Bai, D., 2017. Synthesis and characterization of Zn-Ti

590   layered double hydroxide intercalated with cinnamic acid for cosmetic application. J. Phys.

591   Chem. Solids 107, 62–67. https://doi.org/10.1016/j.jpcs.2017.02.018

592   Liang, X., Zang, Y., Xu, Y., Tan, X., Hou, W., Wang, L., Sun, Y., 2013. Sorption of metal cations on

593   layered double hydroxides. Colloids Surfaces A Physicochem. Eng. Asp. 433, 122–131.

594   https://doi.org/https://doi.org/10.1016/j.colsurfa.2013.05.006

595   Liu, C., Zhang, Z., Zhai, X., Wang, X., Gui, J., Zhang, C., Zhu, Y., Li, Y., 2019. Synergistic effect between

596   copper and different metal oxides in the selective hydrogenolysis of glucose. New J. Chem. 43,

597   3733–3742. https://doi.org/10.1039/C8NJ05815F

598   Luo, M.-F., Fang, P., He, M., Xie, Y.-L., 2005. In situ XRD, Raman, and TPR studies of CuO/Al2O3

599   catalysts for CO oxidation. J. Mol. Catal. A Chem. 239, 243–248.

600   https://doi.org/https://doi.org/10.1016/j.molcata.2005.06.029

601   Marchi, A.J., Apesteguía, C.R., 1998. Impregnation-induced memory effect of thermally activated

602   layered double hydroxides. Appl. Clay Sci. 13, 35–48.

603   https://doi.org/https://doi.org/10.1016/S0169-1317(98)00011-8

604   Mejía-Centeno, I., Castillo, S., Fuentes, G.A., 2012. Enhanced emissions of NH3, N2O and H2 from a

605   Pd-only TWC and supported Pd model catalysts: Light-off and sulfur level studies. Appl. Catal. B

606   Environ. 119–120, 234–240. https://doi.org/https://doi.org/10.1016/j.apcatb.2012.02.030

607 Mista, W., Zawadzki, M., Grabowska, H., 2003. Hydrothermal preparation of CuO-ZnAl2O4 catalyst

608   for phenol ortho-alkylation with methanol: effect of the calcination temperature on the

609   catalytic performance. Res. Chem. Intermed. 29, 137–146.

610   https://doi.org/10.1163/156856703321505030

611 Mrad, R., Cousin, R., Saliba, N.A., Tidahy, L., Siffert, S., 2015. Degradation of VOCs and NOx over

612   Mg(Cu)–AlFe mixed oxides derived from hydrotalcite-like compounds. Comptes Rendus Chim.

613   18, 351–357. https://doi.org/http://dx.doi.org/10.1016/j.crci.2014.08.005

614 Nevalainen, P., Kinnunen, N.M., Kirveslahti, A., Kallinen, K., Maunula, T., Keenan, M., Suvanto, M.,

615   2018. Formation of NH3 and N2O in a modern natural gas three-way catalyst designed for

616   heavy-duty vehicles: the effects of simulated exhaust gas composition and ageing. Appl. Catal. A

617   Gen. 552, 30–37. https://doi.org/https://doi.org/10.1016/j.apcata.2017.12.017

618 Obalová, L., Karásková, K., Jirátová, K., Kovanda, F., 2009. Effect of potassium in calcined Co–Mn–Al

619   layered double hydroxide on the catalytic decomposition of N2O. Appl. Catal. B Environ. 90,

620   132–140. https://doi.org/http://dx.doi.org/10.1016/j.apcatb.2009.03.002

621 Obalová, L., Pacultová, K., Balabánová, J., Jirátová, K., Bastl, Z., Valášková, M., Lacný, Z., Kovanda, F.,

622   2007. Effect of Mn/Al ratio in Co-Mn-Al mixed oxide catalysts prepared from hydrotalcite-like

623   precursors on catalytic decomposition of N2O. Catal. Today.

624   https://doi.org/10.1016/j.cattod.2006.08.027

625 Okamoto, Y., Gotoh, H., 1997. Copper-zirconia catalysts for NO◻CO reactions. Catal. Today 36, 71–79.

626   https://doi.org/10.1016/S0920-5861(96)00198-8

627 Okamoto, Y., Gotoh, H., Hishida, K., Aritani, H., Tanaka, T., Yoshida, S., 1997. Surface copper-TiO2

628   interaction species for NO◻CO reactions. Appl. Surf. Sci. 121–122, 509–512.

629   https://doi.org/10.1016/S0169-4332(97)00355-3

630   Pacultová, K., Karásková, K., Kovanda, F., Jirátová, K., Šrámek, J., Kustrowski, P., Kotarba, A.,

631   Chromčáková, Ž., Kočí, K., Obalová, L., 2016. K-Doped Co–Mn–Al Mixed Oxide Catalyst for N2O

632   Abatement from Nitric Acid Plant Waste Gases: Pilot Plant Studies. Ind. Eng. Chem. Res. 55,

633   7076–7084. https://doi.org/10.1021/acs.iecr.6b01206

634   Patel, A., Shukla, P., Chen, J., Rufford, T.E., Wang, S., Rudolph, V., Zhu, Z., 2015. Structural sensitivity

635   of mesoporous alumina for copper catalyst loading used for NO reduction in presence of CO.

636   Chem. Eng. Res. Des. 101, 27–43. https://doi.org/10.1016/J.CHERD.2015.03.027

637   Patel, A., Shukla, P., Pan, G.T., Chong, S., Rudolph, V., Zhu, Z., 2017. Influence of copper loading on

638   mesoporous alumina for catalytic NO reduction in the presence of CO. J. Environ. Chem. Eng. 5,

639   2350–2361. https://doi.org/10.1016/J.JECE.2017.04.035

640   Pérez, M.R., Pavlovic, I., Barriga, C., Cornejo, J., Hermosín, M.C., Ulibarri, M.A., 2006. Uptake of Cu2+,

641   Cd2+ and Pb2+ on Zn–Al layered double hydroxide intercalated with edta. Appl. Clay Sci. 32,

642   245–251. https://doi.org/https://doi.org/10.1016/j.clay.2006.01.008

643   Prevot, V., Briois, V., Cellier, J., Forano, C., Leroux, F., 2008. An in-situ investigation of LDH–acetate

644   prepared in polyol, under moderate thermal treatment. J. Phys. Chem. Solids 69, 1091–1094.

645   https://doi.org/https://doi.org/10.1016/j.jpcs.2007.10.051

646   Reichle, W.T., Kang, S.Y., Everhardt, D.S., 1986. The nature of the thermal decomposition of a

647   catalytically active anionic clay mineral. J. Catal. 101, 352–359.

648   https://doi.org/https://doi.org/10.1016/0021-9517(86)90262-9

649   Richardson, M.C., Braterman, P.S., 2009. Cation exchange by anion-exchanging clays: the effects of

650   particle aging. J. Mater. Chem. 19, 7965–7975. https://doi.org/10.1039/B908516E

651   Ruiz Puigdollers, A., Schlexer, P., Tosoni, S., Pacchioni, G., 2017. Increasing Oxide Reducibility: The

652   Role of Metal/Oxide Interfaces in the Formation of Oxygen Vacancies. ACS Catal. 7, 6493–6513.

653   https://doi.org/10.1021/acscatal.7b01913

654   Saber, O., Tagaya, H., 2008. Preparation and intercalation reactions of nano-structural materials, Zn-

655   Al-Ti LDH. Mater. Chem. Phys. https://doi.org/10.1016/j.matchemphys.2007.10.024

656   Saber, O., Tagaya, H., 2003. New Layered Double Hydroxide, Zn-Ti LDH: Preparation and Intercalation

657   Reactions. J. Incl. Phenom. 45, 109–116.

658   Saber, O., Zaki, T., 2014. Carbon monoxide oxidation using Zn--Cu--Ti hydrotalcite-derived catalysts. J.

659   Chem. Sci. 126, 981–988. https://doi.org/10.1007/s12039-014-0642-8

660   Schön, A., Dacquin, J.-P., Dujardin, C., Granger, P., 2017. Catalytic Activity and Thermal Stability of

661   LaFe1−xCuxO3 and La2CuO4 Perovskite Solids in Three-Way-Catalysis. Top. Catal. 60, 300–306.

662   https://doi.org/10.1007/s11244-016-0615-x

663   Schön, A., Dacquin, J.-P., Granger, P., Dujardin, C., 2018. Non stoichiometric La1-yFeO3 perovskite-

664   based catalysts as alternative to commercial three-way-catalysts? – Impact of Cu and Rh

665   doping. Appl. Catal. B Environ. 223, 167–176.

666   https://doi.org/https://doi.org/10.1016/j.apcatb.2017.06.026

667   Schön, A., Dujardin, C., Dacquin, J.-P., Granger, P., 2015. Enhancing catalytic activity of perovskite-

668   based catalysts in three-way catalysis by surface composition optimisation. Catal. Today 258,

669   543–548. https://doi.org/https://doi.org/10.1016/j.cattod.2014.11.002

670   Seftel, E., Popovici, E., Mertens, M., Witte, K. De, Tendeloo, G. Van, Cool, P., Vansant, E.F., 2008. Zn–

671   Al layered double hydroxides: Synthesis, characterization and photocatalytic application.

672   Microporous Mesoporous Mater. 113, 296–304.

673   https://doi.org/https://doi.org/10.1016/j.micromeso.2007.11.029

674   Seftel, E.M., Ciocarlan, R.G., Michielsen, B., Meynen, V., Mullens, S., Cool, P., 2018. Insights into

675   phosphate adsorption behavior on structurally modified ZnAl layered double hydroxides. Appl.

676   Clay Sci. 165, 234–246. https://doi.org/https://doi.org/10.1016/j.clay.2018.08.018

677   Seftel, E.M., Popovici, E., Mertens, M., Van Tendeloo, G., Cool, P., Vansant, E.F., 2008. The influence

678   of the cationic ratio on the incorporation of Ti4+ in the brucite-like sheets of layered double

679   hydroxides. Microporous Mesoporous Mater. 111, 12–17.

680   https://doi.org/10.1016/j.micromeso.2007.07.008

681   Severino, F., Brito, J.L., Laine, J., Fierro, J.L.G., Agudo, A.L., 1998. Nature of Copper Active Sites in the

682   Carbon Monoxide Oxidation on CuAl2O4and CuCr2O4Spinel Type Catalysts. J. Catal. 177, 82–95.

683   https://doi.org/10.1006/JCAT.1998.2094

684   Stanimirova, T., Balek, V., 2008. Characterization of Mg-Al-CO3 Layered Double Hydroxides prepared

685   by re-hydration of Mg-Al mixed oxide. J. Therm. Anal. Calorim. 94, 477–481.

686   Van Der Grift, C.J.G., Mulder, A., Geus, J.W., 1990. Characterization of silica-supported copper

687   catalysts by means of temperature-programmed reduction. Appl. Catal. 60, 181–192.

688   https://doi.org/10.1016/S0166-9834(00)82181-8

689   Van Everbroeck, T., Ciocarlan, R.-G., Hoey, W. Van, Mertens, M., Cool, P., 2020. Copper-Containing

690   Mixed Metal Oxides (Al, Fe, Mn) for Application in Three-Way Catalysis. Catalysts 10, 1344.

691   https://doi.org/10.3390/catal10111344

692   Vandenberghe, R.E., Legrand, E., Scheerlinck, D., Brabers, V.A.M., 1976. Neutron diffraction study of

693   the cation ordering in Cu1.5Mn1.5O4 and CuMg0.5Mn1.5O4. Acta Crystallogr. Sect. B 32, 2796–

694   2798. https://doi.org/10.1107/S056774087600890X

695   Vandenberghe, R.E., Robbrecht, G.G., Brabers, V.A.M., 1973. On the stability of the cubic spinel

696   structure in the system Cu◻Mn◻O. Mater. Res. Bull. 8, 571–579. https://doi.org/10.1016/0025-

697   5408(73)90134-7

698   Vepřek, S., Cocke, D.L., Kehl, S., Oswald, H.R., 1986. Mechanism of the deactivation of Hopcalite

699   catalysts studied by XPS, ISS, and other techniques. J. Catal. 100, 250–263.

700   https://doi.org/10.1016/0021-9517(86)90090-4

701 Wang, J., Chen, H., Hu, Z., Yao, M., Li, Y., 2015. A Review on the Pd-Based Three-Way Catalyst. Catal.

702 Rev. 57, 79–144. https://doi.org/10.1080/01614940.2014.977059

703 Weng, L.T., Delmon, B., 1992. Phase cooperation and remote control effects in selective oxidation

704 catalysts. Appl. Catal. A, Gen. https://doi.org/10.1016/0926-860X(92)80093-R

705 Wu, J., Dacquin, J.P., Cordier, C., Dujardin, C., Granger, P., 2019. Optimization of the Composition of

706 Perovskite Type Materials for Further Elaboration of Four-Way Catalysts for Gasoline Engine.

707 Top. Catal. 62, 368–375. https://doi.org/10.1007/s11244-018-1083-2

708 Xin, Q., Papavasilou, A., Boukos, N., Glisenti, A., Li, J.P.H., Yang, Y., Philippopoulos, C.J., Poulakis, E.,

709 Katsaros, F.K., Meynen, V., Cool, P., 2016. Preparation of CuO/SBA-15 catalyst by the modified

710 ammonia driven deposition precipitation method with a high thermal stability and an efficient

711 automotive CO and hydrocarbons conversion. Appl. Catal. B Environ.

712 https://doi.org/10.1016/j.apcatb.2017.03.071

713 Yuan, D., Li, X., Zhao, Q., 2013. Preparation and characterization of Ni-Ti-O mixed oxide for selective

714 catalytic reduction of NO under lean-burn conditions. Chinese J. Catal. 34, 1449–1455.

715 https://doi.org/http://dx.doi.org/10.1016/S1872-2067(12)60614-7

716 Yuan, D., Li, X., Zhao, Q., Zhao, J., Tadé, M., Liu, S., 2014. A novel CuTi-containing catalyst derived

717 from hydrotalcite-like compounds for selective catalytic reduction of NO with C3H6 under lean-

718 burn conditions. J. Catal. 309, 268–279. https://doi.org/10.1016/j.jcat.2013.09.010

719 Zhao, Q., Yan, Z., Chen, C., Chen, J., 2017. Spinels: Controlled Preparation, Oxygen

720 Reduction/Evolution Reaction Application, and Beyond. Chem. Rev. 117, 10121–10211.

721 https://doi.org/10.1021/acs.chemrev.7b00051

722

723

724

Supplementary information

Reagents

727 All chemicals were purchased from Sigma-Aldrich/Merck and used without any further purification.

728 The used chemicals are: $Cu(NO_3)_2.3H_2O$ (99.0 wt%), $Zn(NO_3)_2.6H_2O$ (99 wt%), $Al(NO_3)_3.9H_2O$ (99 wt%),

729 $TiCl_4$ 99.9 wt%), $MnCl_2$ (97.0 wt%), NaOH (98.5 wt%), Na_2CO_3 (99.95-100.05 wt%), Copper acetate (98

730 wt%).

Sherrer equation:

732 The average crystallite size was estimated using the Scherrer equation:

$$d = \frac{K\lambda}{\beta \cos(\theta)}$$

734 Where, d = crystallite size, λ = the wavelength of the X-ray source (0.15406 nm), β = the full

735 width at half maximum of the chosen diffraction peak (2θ), ϑ = Bragg angle and K = the shape

736 constant chosen as 0.9. Using this equation, the morphological effects and disorder to

737 reflection widths were not taken into account, so the obtained values were merely used for

738 relative comparison of the materials (Hargreaves, 2016).

739

Catalytic activity measurements

741 The experiment consisted of four consecutive heating (at 5°C/min) and cooling cycles between 110

742 and 550°C, in different conditions (stoichiometric, lean, rich), preceded by a pre-treatment at 600°C

743 in air and under stoichiometric condition.
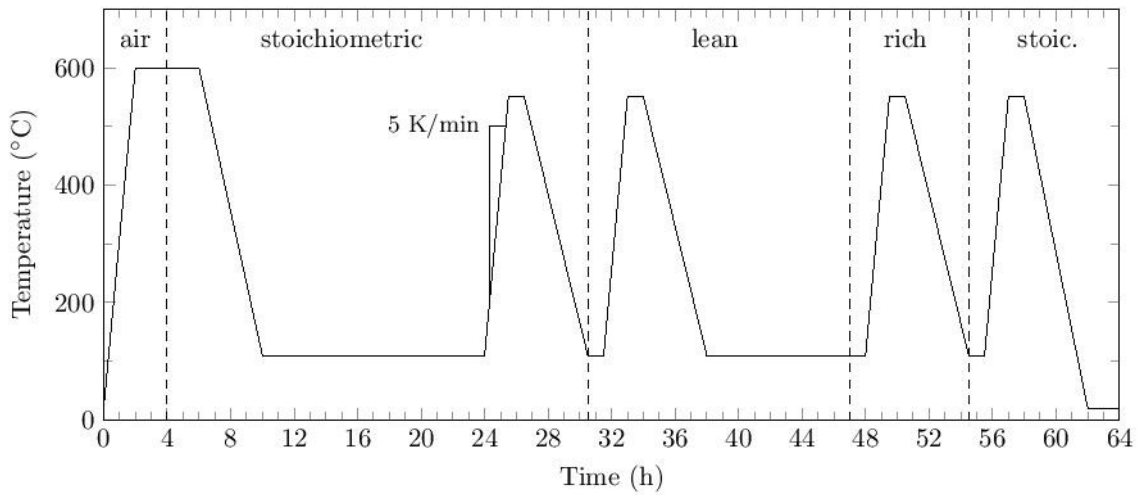
Supplementary Figure 1: Procedure for catalytic testing.

The gas composition for each of the conditions is described in Supplementary **¡Error! No se encuentra el origen de la referencia.**. The flow rate was adjusted to correspond to a Gas Hourly Space Velocity of 60 000 mL h^{-1} g^{-1}. The composition of the gas at the outlet was monitored by a Thermo Scientific 42i-HL chemiluminescence analyzer for NOx detection and an Agilent Technologies 490 micro GC for the quantification of N_2, N_2O, H_2, CO, propane, propene and CO_2. The displayed conversions were calculated from the heating cycles, using the following formula:

$$X_i(\%) = \left(1 - \frac{[i]}{[i]_0}\right) . 100$$

Where X_i = the conversion of compound i, $[i]$ is the concentration of i at the outlet, and $[i]_0$ is the inlet concentration of i.

The concentration of NH_3 was calculated using the following formula assuming that all NO not converted to N_2 or N_2O leads to NH_3:

$$[NH_3] = [NO]_0 - ([NO] + 2 \ [N_2] + 2 \ [N_2O])$$

The selectivity of NO towards N_2 (S_{N_2}), N_2O (S_{N_2O}) and NH_3 (S_{NH_3}) were calculated as follows:

$$S_{N_2} = \frac{2 \ [N_2]}{[NO]_0 - [NO]}$$

$$S_{N_2O} = \frac{2\ [N_2O]}{[NO]_0 - [NO]}$$

$$S_{NH_3} = \frac{[NH_3]}{[NO]_0 - [NO]}$$

The yield (Y_i) was determined as:

$$Y_i = X_i \cdot S_i$$

Condition/Gas(vol%)	NO	CO	C_3H_6	C_3H_8	H_2	O_2	CO_2	H_2O	He
Stoichiometric	0.1	0.7	0.045	0.022	0.23	0.73	15	10	Balance
Lean	0.1	0.5	0.03	0.015	0.17	0.90	15	10	Balance
Rich	0.1	0.9	0.06	0.030	0.30	0.55	15	10	Balance

Supplementary Table 3: Gas composition of the different conditions during the catalytic experiment.

The specific reaction rate (Spec. RR) is calculated by dividing the reaction rate (RR) by the BET specific surface area (SSA):

$$Spec. RR = \frac{RR}{SSA}$$

The reaction rate (RR) is calculated as follows (example for CO):

$$RR_{CO} = \frac{[CO]_0 \cdot X_{CO} \cdot F \cdot p}{T \cdot R \cdot g_{cat}}$$

F is the total flow rate, p the pressure (1.013 bar), T the temperature, R the gas constant. g_{cat} the weight of the catalyst.

The turnover frequency is calculated by dividing the reaction rate (RR) by the number of moles Cu in the catalyst, based on the SEM-EDX results:

$$TOF = \frac{RR}{\# \, mol \, CuO/g_{cat}}$$

Textural characteristics of the catalysts

The values for the BET specific surface area (SSA) of the different synthesized materials are presented inSupplementary table 2. The evolution of the surface area through the different synthesis steps can be deduced from left to right. Isotherms and additional textural properties are presented in Supplementary figure 2 to 7. For the initial materials, the copper-containing LDHs have each time a higher surface area than their non-copper containing LDHs (e. g. ZCA vs. ZA or ZCAT vs. ZAT). At the same time, titanium and manganese presence in the materials generally tends to increase the surface area (e. g. the case of ZAT, ZCAT, MZAT, MCAT or MT). Comparing the three-way catalysts obtained by the thermal treatment at 600°C to the initial ones, it can be concluded that the results are quite divergent; ZA, ZCA and MA increase their surface area along with the synthesis steps, while the others decrease their surface area along the process.

SSA (m^2/g)	Non-calcined	Calcined 400°C	Reconstructed	Three-way catalysts (calcined 600°C)
ZA	38	78	14	66
ZCA	45	-	-	63
ZAT	148	105	58	80
ZCAT	179	-	-	54

38

MZAT	195	130	113	46
MCAT	259	-	-	117
MA	66	188	98	73
MT	159	157	60	28

Supplementary table 2: BET specific surface area (SSA) of the synthesized materials in the different stages (non-calcined material, calcined at 400°C, after reconstruction in Cu-containing aqueous solutions and the obtained three-way catalysts produced by the calcination at 600°C).
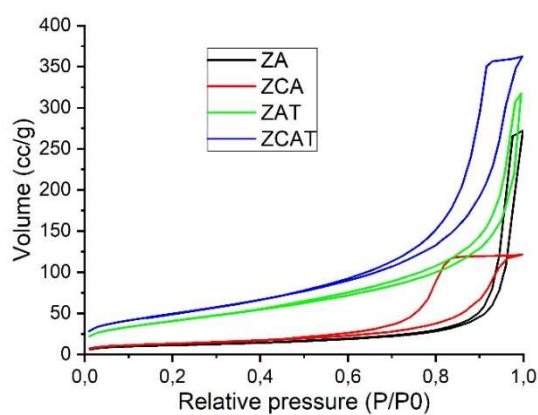
Supplementary figure 2: N₂-sorption isotherm of the materials prepared by co-precipitation (ZA, ZCA, ZAT, ZCAT).
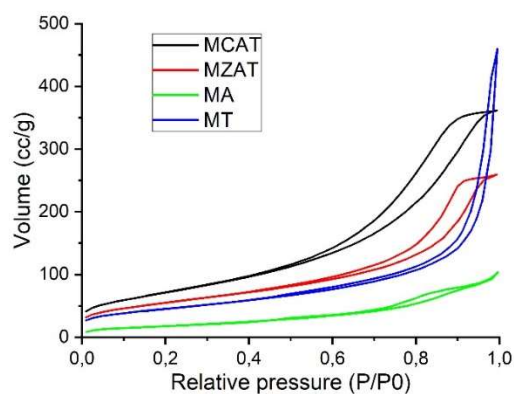
Supplementary figure 3: N₂-sorption isotherm of the materials prepared by co-precipitation (MCAT, MZAT, MA, MT).
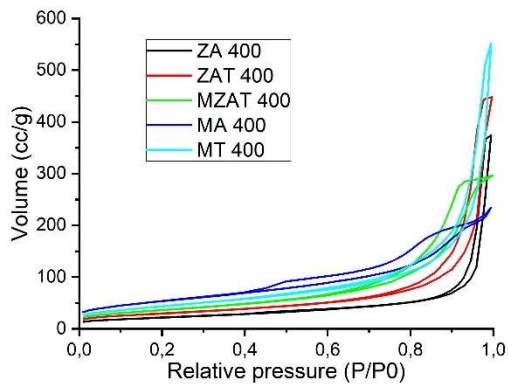
805

806   *Supplementary figure 4: N₂-sorption isotherm of the materials calcined at 400 °C.*

807
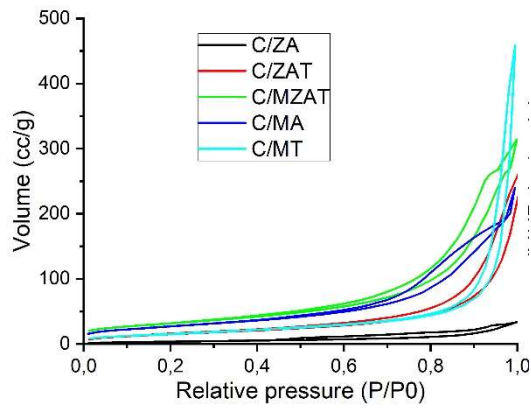
808

809   *Supplementary figure 5: N₂-sorption isotherm of the materials after impregnation with Cu by the reconstruction method.*

810
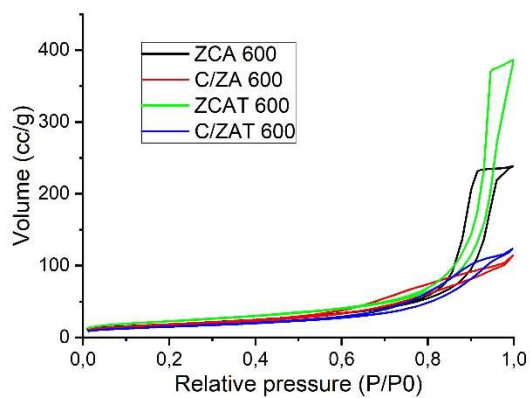
811

812   *Supplementary figure 6: N₂-sorption isotherm of the final materials calcined at 600°C (ZCA 600, C/ZA 600, ZCAT 600, C/ZAT*
813   *600).*

814
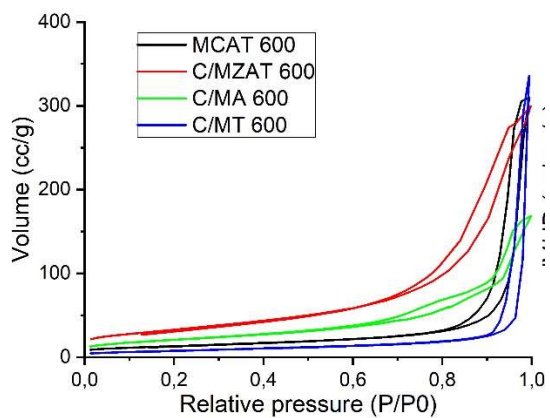
815

816 *Supplementary figure 7: N$_2$-sorption isotherm of the final materials calcined at 600°C (MCAT 600, C/MZAT 600, C/MA 600,*
817 *C/MT 600).*

818

819

EDS mapping

820
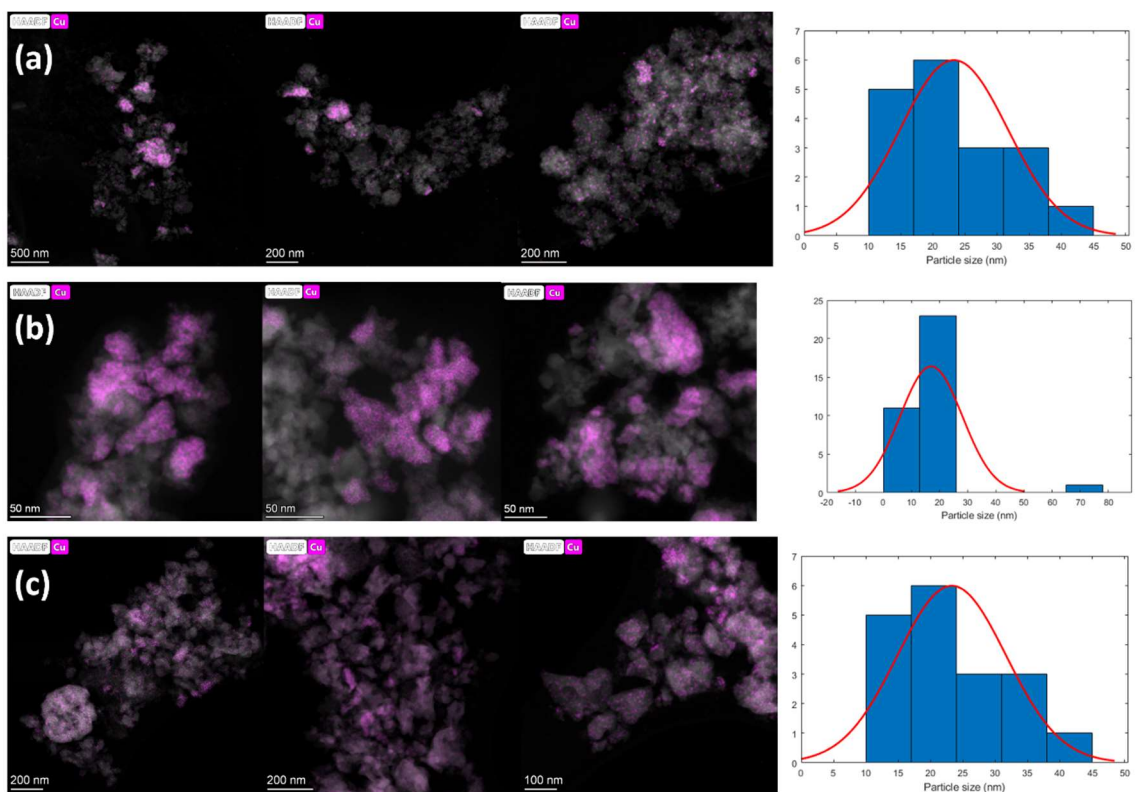
821

822 *Supplementary figure 8: HAADF-STEM image with the EDS Cu mapping of different areas and CuO nanoparticles size*
823 *distribution of (a) ZCAT-600, (b) C/ZAT-600 and (c) C/MA-600.*

824

825

Catalytic activity testing

Stoic 1	Temperature 50 % conversion			max. NO conv.	temp. for max. NO conv.
	CO	C_3H_6	C_3H_8		
ZCA-600	293	381	n.r.	1.2	327
C/ZA-600	329	436	n.r.	2.4	424
ZCAT-600	389	457	n.r.	4.9	453
C/ZAT-600	325	356	552	8	387
MCAT-600	314	534	577	2.4	576
C/MZAT-600	276	331	549	8.1	341
C/MA-600	239	409	497	11.7	522
C/MT-600	269	528	n.r.	9.5	429
Comm. TWC	217	262	454	47.1	285
0.5% Pd/CeZrO$_2$	136	177	532	27	232

Supplementary table 3: temperatures at which 50 % conversion is reached and maximal NO conversion in the first stoichiometric cycle. N.r. = not reached.

Under lean conditions (Supplementary Figure 9), one would expect lower NO conversions and higher conversions of CO and the organic compounds, due to the relatively higher amount of O_2 present. The maximal NO conversion is indeed lower (< 5%), except for C/MA-600, which still manages to convert up to 10.7%. CO and propene conversions are very comparable to the first stoichiometric cycle, while propane conversion is slightly improved.

835
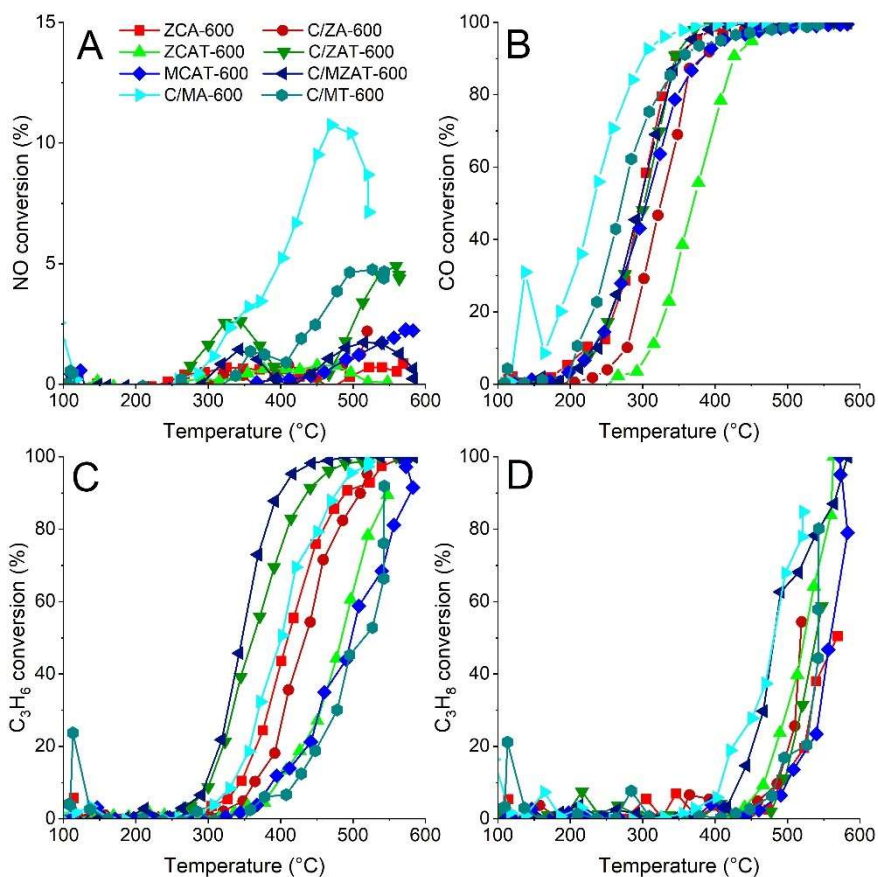
Supplementary Figure 9: Temperature programmed conversion curves under lean conditions, A: NO conversion, B: CO
837   *conversion, C: propene conversion, D: propane conversion.*

838

	Temperature 50% conversion			max. NO conv.	temp. for max. NO conv.
Lean	CO	C_3H_6	C_3H_8		
ZCA-600	297	410	568	0.9	569
C/ZA-600	325	434	518	2.2	520
ZCAT-600	370	484	539	0.8	451
C/ZAT-600	302	362	523	4.9	560

MCAT-600	311	525	570	2.3	573
C/MZAT-600	296	347	481	1.7	515
C/MA-600	231	401	481	10.7	470
C/MT-600	271	515	542	4.8	527
Comm. TWC	198	213	466	17.5	305
0.5% Pd/CeZrO$_2$	188	247	521	18	368

839   *Supplementary Table 4: temperatures at which 50% conversion is reached and maximal NO conversion in the lean cycle. N.r.*

840   *= not reached.*

841

842   In the rich condition (Supplementary Figure 10), less O$_2$ is present so NO is more likely to

843   oxidise CO and the hydrocarbons. This is clearly the case here, as NO conversion reaches

844   nearly 100% in all the cases. C/MZAT-600 stands out with the lowest T$_{50}$, while ZCAT-600 and

845   MCAT-600 perform considerably worse. The T$_{50}$ for CO and propene are slightly higher, but

846   the conversion of propane is definitely worse as none of the studied three-way catalysts are

847   able to convert up to 50% propane under 550°C.
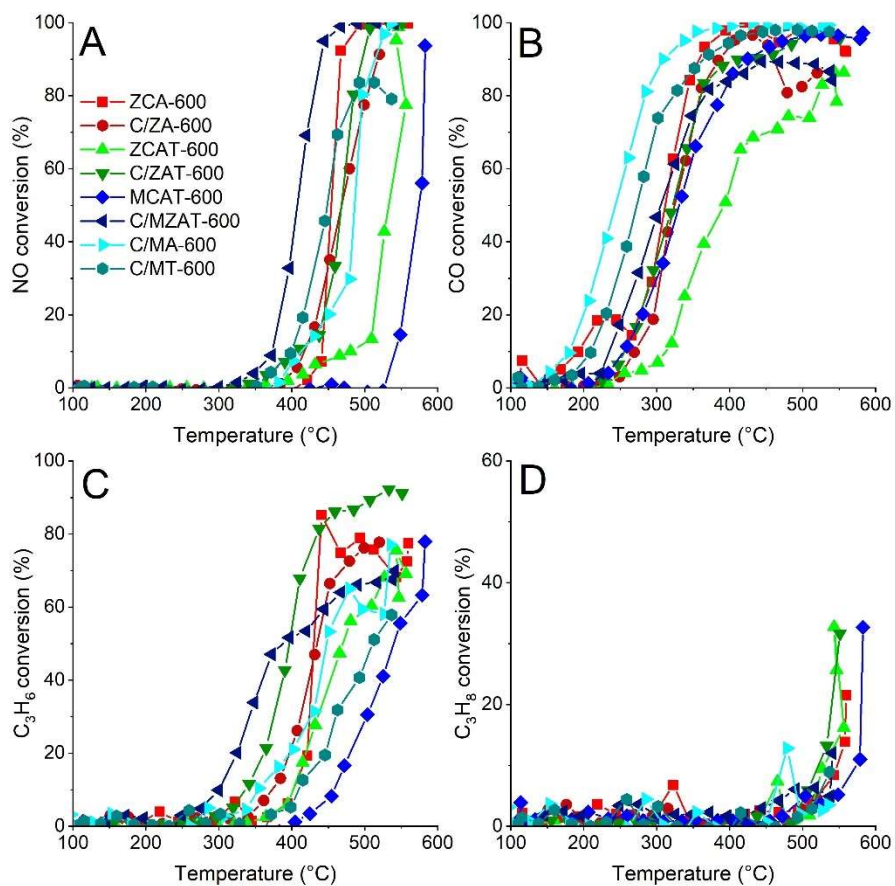
848

849   Supplementary Figure 10: Temperature programmed conversion curves under rich conditions, A: NO conversion, B: CO

850   conversion, C: propene conversion, D: propane conversion.

851

| Rich | Temperature 50% conversion | | | |
	CO	C_3H_6	C_3H_8	NO
ZCA-600	312	430	n.r.	454
C/ZA-600	325	435	n.r.	468
ZCAT-600	392	470	n.r.	533
C/ZAT-600	322	396	n.r.	468
MCAT-600	331	540	n.r.	574
C/MZAT-600	306	388	n.r.	407

C/MA-600	243	448	n.r.	486
C/MT-600	273	511	n.r.	449
Comm. TWC	240	333	441	286
0.5% Pd/CeZrO$_2$	137	352	456	136

Supplementary Table 54: temperatures at which 50% conversion is reached in the rich cycle. N.r. = not reached.

Propene and propane discussion

The general trend that a higher T_{50} is associated with the presence of larger CuO crystallite sizes is not observed from the propene conversion profiles. The addition of manganese in the three-way catalysts does not improve the propene conversion much. The three-way catalysts C/ZAT-600 and C/MZAT-600 perform the best, showing every time the lowest T_{50} and achieving more than 90% conversion at the lowest temperatures, while the lowest catalytic conversions are found with MCAT-600 and C/MT-600. C/MA-600 on the other hand performs better and its profile is even similar to C/MZAT-600 in the last stoichiometric cycle. This demonstrates again that using alumina certainly represents an advantage over titania, probably because it behaves better as a mesoporous support than titania which further crystallizes into a rutile structure during the catalytic tests. This assumption is also supported by the superior activity of the C/ZAT-600 and C/MZAT-600, in which the solid state reaction between the ZnO and TiO$_2$ leads to the formation of Zn$_2$TiO$_4$ thus inhibiting the crystallisation into a rutile phase.

Not much distinction can be made between the different three-way catalysts in the propane conversion profiles. Only C/MA-600 clearly shows the best performances compared to all the studied three-way catalysts, with its much lower T_{50}. Similarly as hypothesized for the CO and

872 propene conversion, this may be assigned to the presence of the amorphous alumina which

873 inhibits agglomeration of the copper and manganese, while the surface area enhances their

874 dispersion.

875

876 The purpose of the second stoichiometric cycle is to compare it with the first one, in order to

877 check whether the performance of the catalysts is declining or not after this long dynamic

878 procedure. For all the samples, except C/MA-600, the maximal NO conversion is lower, under

879 6%. Similar CO conversions as in the first catalytic cycle are observed. Surprisingly, some

880 catalysts even have a lower T_{50} compared to the first catalytic cycle. For example, the T_{50} for

881 MCAT-600 is 62°C lower than in the first cycle (314°C and 252°C). For the propene conversion

882 the situation is the same. There is a difference of 114°C for MCAT-600 between the first and

883 the second catalytic cycle (534°C and 420°C), while the propane conversion is very similar

884 between the two catalytic cycles.

885

Stoic 2	Temperature 50% conversion			max. NO conv.	temp. for max. NO conv.
	CO	C_3H_6	C_3H_8		
ZCA-600	310	384	567	1.2	371
C/ZA-600	346	370	n.r.	5.8	395
ZCAT-600	390	459	n.r.	5.6	432
C/ZAT-600	301	332	561	4.2	348

MCAT-600	252	420	568	2	583
C/MZAT-600	274	353	524	1.4	332
C/MA-600	239	353	464	9.5	527
C/MT-600	255	452	n.r.	2.8	337
Comm. TWC	228	268	456	52	358
0.5% Pd/CeZrO$_2$	157	231	507	39	259

886 *Supplementary Table 6: Temperatures at which 50% conversion is reached and maximal NO conversion in the second*

887 *stoichiometric cycle N.r. = not reached.*
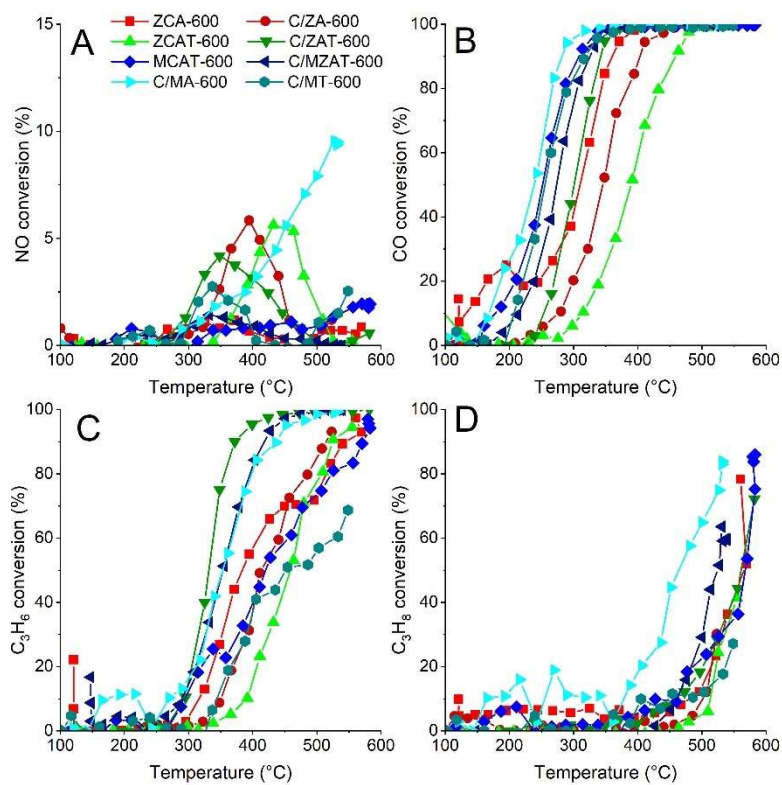
889 *Supplementary Figure 11: Temperature programmed conversion curves under stoichiometric conditions, second cycle, A: NO*

890 *conversion, B: CO conversion, C: propene conversion, D: propane conversion.*

893 NO conversion discussion

894 In stoichiometric and lean conditions, all NO reduced during the test is selectively converted

895 to N_2. In the rich condition, NH_3 and N_2O are also formed through side reactions. The selectivity

896 of the NO conversion in the rich condition for all the catalysts is displayed in Supplementary

897 Figure 12 and the corresponding yields can be found in Supplementary Figure 13. The

898 selectivity towards N_2O is very low for all the studied three-way catalysts, however, the

899 selectivities towards N_2 and NH_3 are almost equal at high temperatures. Overall, the yields

900 towards N_2 are higher for the catalysts containing titanium (ZCAT-600, C/ZAT-600, C/MT) as

901 compared to the catalysts that do not contain titanium (ZCA-600, C/ZA-600, C/MA).

902
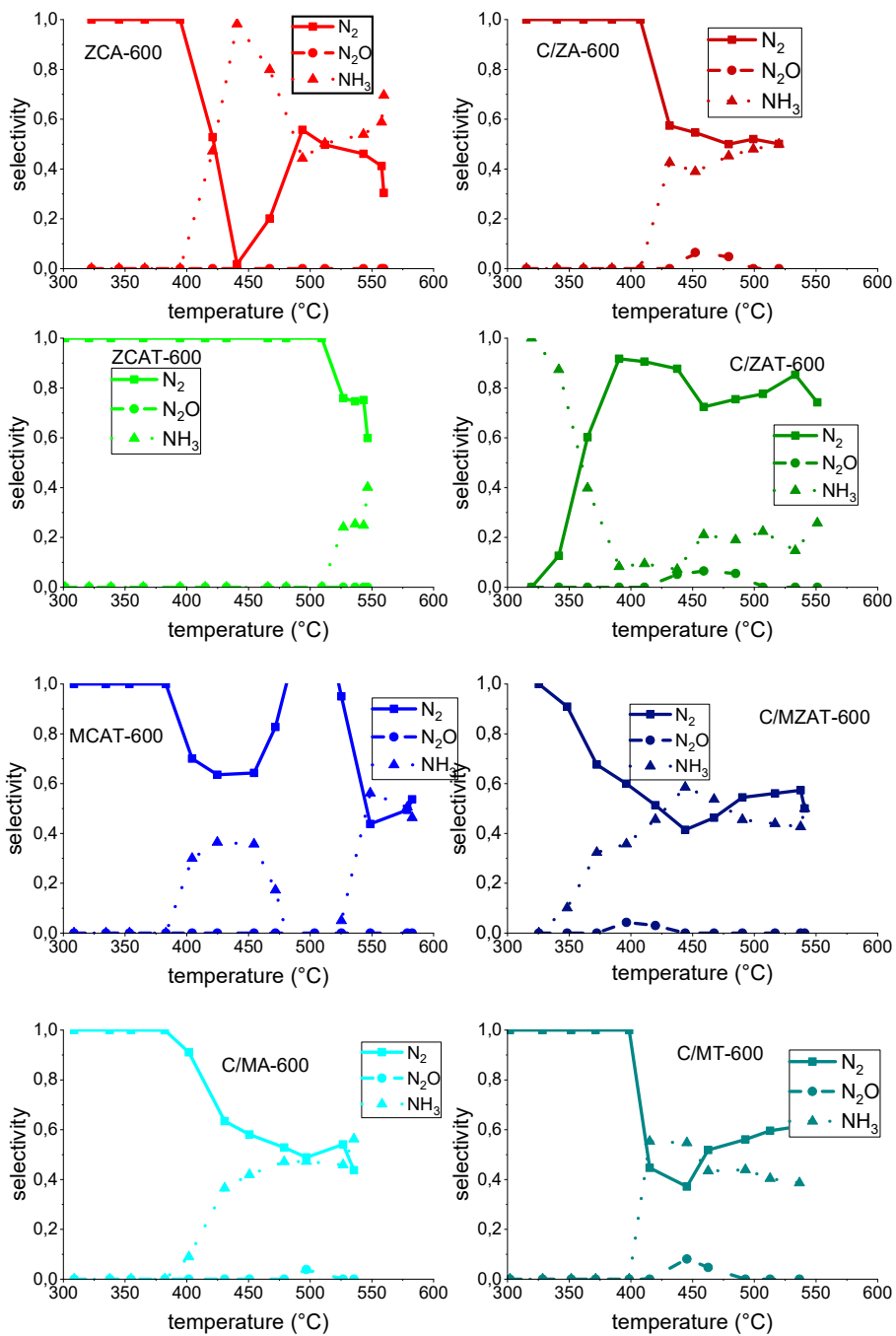
903

904   *Supplementary Figure 12: Selectivity of NO towards N_2, N_2O and NH_3 during the rich condition for all catalysts.*

905

906

907
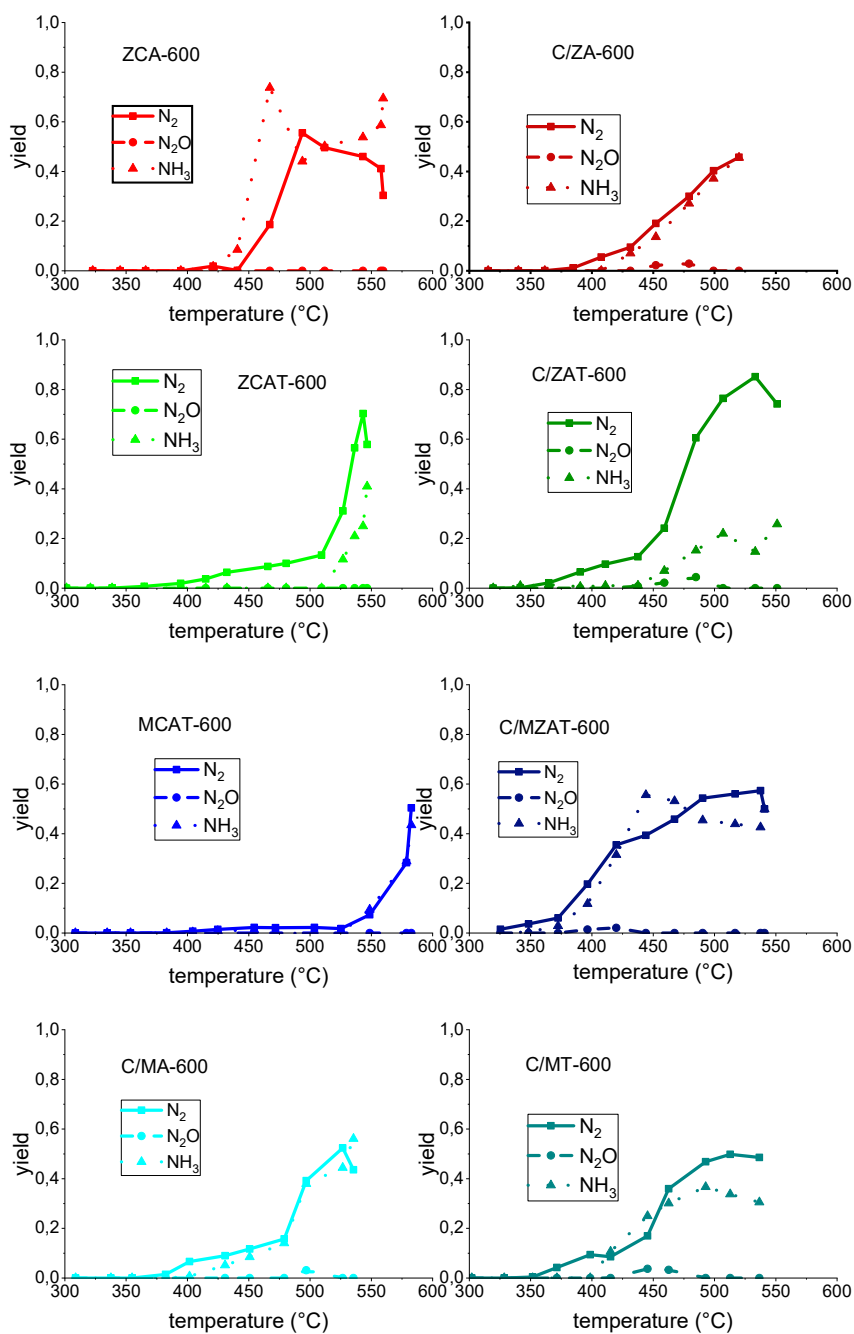
909   *Supplementary Figure 13: Yield of NO conversion towards N_2, N_2O and NH_3 for all catalysts.*

910   In stoichiometric and lean conditions, the NO conversion profiles exhibit typical volcano plots.

911   This occurs because the selectivity for the reactions with NO drops for reactions with O_2. In

912   this way, four local maxima for the four different reactants (H_2, CO, propene, propane) can

913   be expected, which explains the often strange shape of the NO conversion profiles. The

914   catalysts used here, under these specific conditions, seem to mainly convert NO with propene

915   or H_2. As an example, for the profile of C/MZAT-600 there is a sharp rise in the NO conversion

916   at around 300°C, which is also the temperature where propene and H_2 conversion starts (H_2

917   conversion profile can be found in Supplementary Figure 14). Analysing the profiles of the first

918   stoichiometric cycle, it suggests that the materials containing titanium produce higher

919   maximal NO conversions. However, while C/MA-600 shows medium conversion at low

920   temperatures, the NO conversion is much higher than for all the other catalysts at high

921   temperatures. This can be related to the propene conversion observed in this case, being less

922   steep than for example C/MZAT-600 and to the propane conversion, which starts at a lower

923   temperature than for the other catalysts. In the lean cycle, the multiple volcano plots are more

924   clear and again, the highest conversion is found for C/MA-600, but C/ZAT and C/MT still stand

925   out to the other catalysts.

926   In the rich conditions, NH_3 formation is also possible (reaction 1) and the selectivity profiles

927   demonstrate that this is certainly the case here. NH_3 formation is also undesired as it is

928   poisonous for the catalyst, corrosive for the system and can form particulate matter (Wang et

929   al., 2015; Nevalainen et al., 2018).

930    $$2\,NO + 5\,H_2 \ \rightarrow\ 2\,NH_3 + 2\,H_2O \quad (1)$$
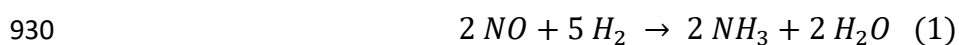
931   However, evaluating the H_2 conversion plots in the rich conditions (Supplementary Figure 15),

932   it can be concluded that the H_2 conversion reaches 100% before the temperature at which the

933   NO conversion starts, mainly due to the reaction with O_2. A source of the extra H_2 required for

934   NH_3 formation can be steam reforming of propene and the water-gas shift reaction (reaction

935   2 and 3) (Mejía-Centeno et al., 2012; Nevalainen et al., 2018).

936    $$C_3H_6 + 3\,H_2O \ \rightarrow\ 3\,CO + 6\,H_2 \quad (2)$$

$$CO + H_2O \rightarrow CO_2 + H_2 \quad (3)$$
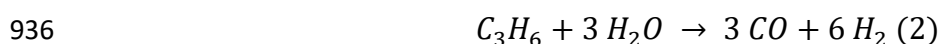
937
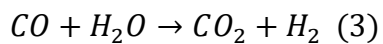
938   As concluded above, the three-way catalysts containing titanium have a higher yield for N_2 at

939   high temperatures (500°C) than their titania-free correspondents. Yuan *et al.* postulate that

940   the higher N_2 selectivity of a copper-titanium mixed oxide is due to the existence of more

941   Lewis sites, which adsorb NO as nitrates on the catalyst surface (Yuan et al., 2014).
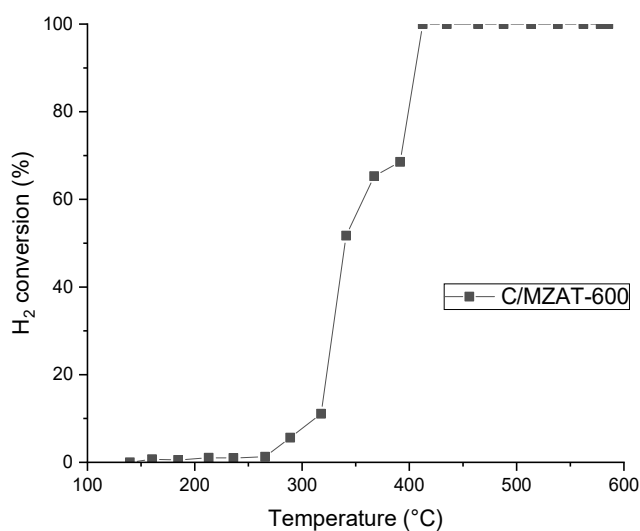
Supplementary Figure 14: H_2 conversion in the first stoichiometric cycle for C/MZAT-600.

943
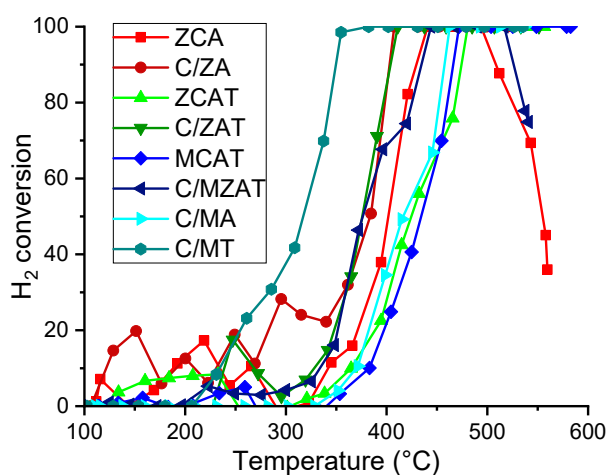
Supplementary Figure 15: H_2 conversion of the materials under rich conditions.

945

946

Specific reaction rates and turnover frequency

The conversion profiles presented earlier are proportional to the reaction rates for 200 mg of catalyst at different temperatures. Reaction rates can however also be expressed based on the specific surface area of the catalyst which makes sense as catalysis happens mostly on the surface. A large surface area will give a catalyst advantage over a catalyst with a smaller surface area. For this reason, a specific reaction rate is defined, which expresses the amount of converted molecules per second per m^2 of catalyst surface area. Specific reaction rate profiles for CO, NO and propene in the first stoichiometric cycle can be found in Supplementary Figure 16Supplementary Figure 17Supplementary Figure 18. C/MT-600 and C/MZAT-600, who were already amongst the best performing catalysts, are standing here even more out from the others due to their relatively lower surface area. This shows again that the titania-containing catalysts have a lot of potential but that the small surface area due the crystallisation of titania is a drawback in these high temperature applications.

Another way to express reaction rates is based on the amount of reactive sites in the catalyst, which is called the turnover frequency (TOF). Here it is assumed that the reactive sites are only the Cu-atoms and that every Cu-atom in the material is accessible and taking part in the catalysis. A more accurate TOF would be probably somewhere between the presented TOF and the specific reaction rate as Cu-atoms buried deep into the bulk of the material will most likely not take part in the reactions. Profiles of the TOFs as a function of temperature for CO, NO and propene in the first stoichiometric cycle can be found as Supplementary Figure 19, 19 and 20. As the Cu content for C/MZAT-600, C/MA-600 and C/MT-600 is much lower and their catalytic performance is very good, they stand out even more from the others in the TOF profiles. This emphasizes the fact that Cu deposited as small particles in a post-synthesis method is much more efficient than in a direct synthesis method.
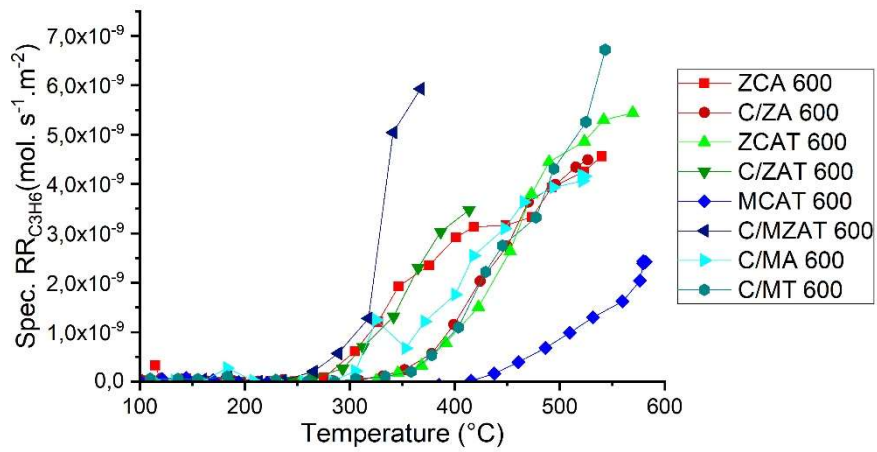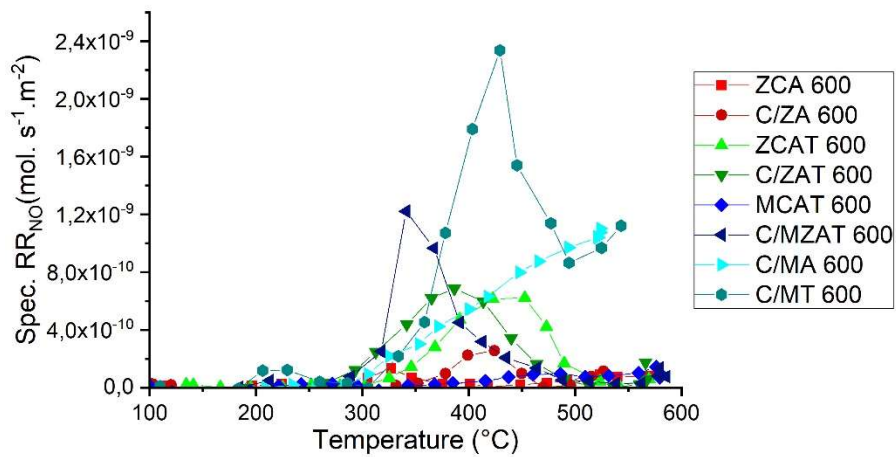
971

972   *Supplementary Figure 16: Specific reaction rates for C_3H_6 during the first stoichiometric cycle.*
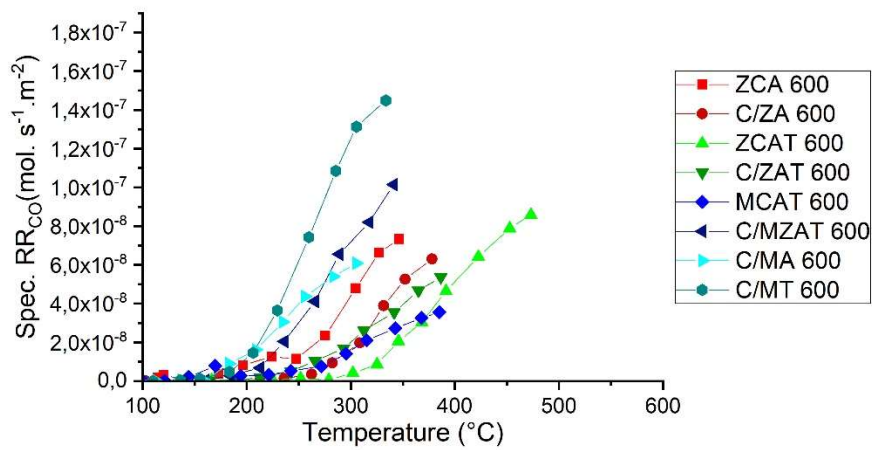
973

974   *Supplementary Figure 17: Specific reaction rates for CO during the first stoichiometric cycle.*
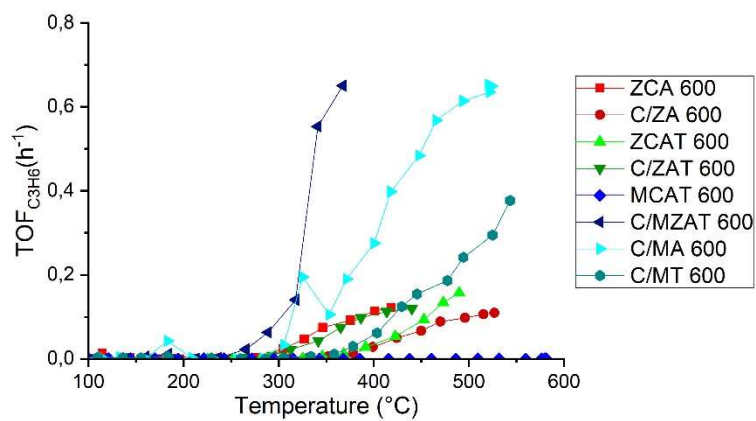

975

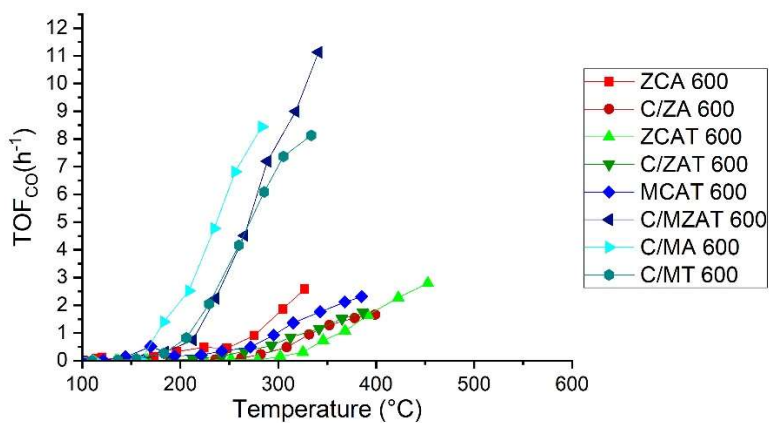976   *Supplementary Figure 18: Specific reaction rates for NO during the first stoichiometric cycle.*
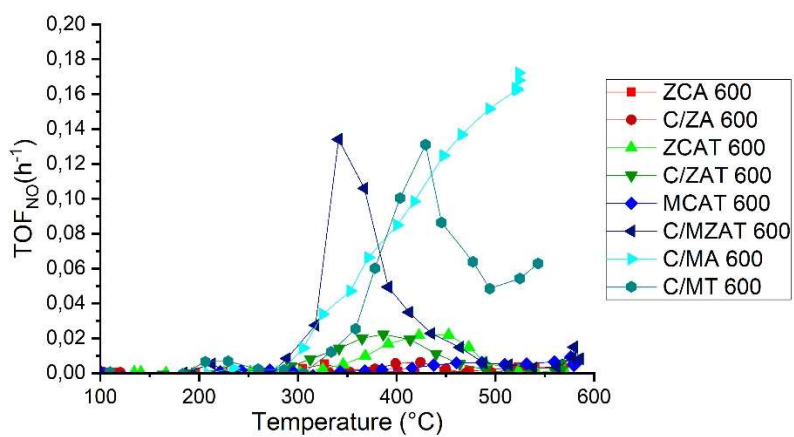
977

978   *Supplementary Figure 19: Turn-over frequencies for C_3H_6 during the first stoichiometric cycle.*

979

980   *Supplementary figure 20 Turn-over frequencies for CO during the first stoichiometric cycle.*

981

982   *Supplementary Figure 21: Turn-over frequencies for NO during the first stoichiometric cycle.*

983

984

Comparison with commercial catalysts

986 The benchmarking of the catalytic results with literature reports is not that straightforward as

987 small differences in the experimental set-up or in the gas feed compositions may lead to

988 significant differences in the catalytic performances. On the other hand, extensive research in

989 the development and testing of three-way catalysts based on $LaFeO_3$ perovskite materials was

990 performed by the group of P. Granger (Schön et al., 2015, 2017, 2018; Wu et al., 2019) where

991 the catalytic testing was done using the same experimental set-up. The best performing non-

992 PGM containing catalyst in those studies is $La_{0.67}Fe_{0.87}Cu_{0.13}O_3$ and has a T_{50} of 232°C for CO

993 and 386°C for propene in the first stoichiometric cycle but in the second stoichiometric cycle

994 this amounts to 255°C and 390°C. The present developed C/MA-600 three-way catalyst shows

995 a comparable performance for CO conversion in the first stoichiometric cycle (T_{50} = 239°C) and

996 is able to maintain this performance in the second stoichiometric cycle (T_{50} = 239°C). The T_{50}

997 of C/MA-600 for the propene conversion is even improving from the first to the second

998 stoichiometric cycle (from 409 to 353°C), performing much better than the reported

999 perovskite type material. Further, ZCA-600, C/ZA-600, C/ZAT-600 and C/MZAT-600 developed

1000 in the present study also show lower T_{50} than the above mentioned perovskite-based catalyst

1001 for propene conversion in the second stoichiometric cycle. Remarkably, the current developed

1002 three-way catalysts manage to reach in some cases almost 10% NO conversion in

1003 stoichiometric conditions, while there is virtually no activity reported using the perovskite

1004 type materials. In conclusion, the main advantages of the catalysts developed in this work are

1005 the great CO and propene conversion abilities, as well as some NO conversion while also

1006 showing a good stability over subsequent catalytic cycles.

1007 Ultimately, to further benchmark the performances of the three-way catalysts developed in

1008 this study, two PGM containing commercial three-way catalysts provided by Johnson Matthey

1009 were tested in the same catalytic conditions, namely a 0.5 wt% Pd loaded onto $CeZrO_2$ (results

1010 included in the Supplementary Figure 22) and a grounded piece of monolith of the commercial

1011 three-way catalytic converter (comm. TWC, results included in Supplementary Figure 23),

1012 respectively. For these commercial catalysts, the catalytic testing was performed in all three

1013 experimental conditions (stoichiometric, lean, rich) as well as in a second stoichiometric cycle.

1014 It can be observed that for C/MA-600, the CO conversion is almost comparable to that of the

1015 commercial TWC, but it is still almost 100°C higher than for $Pd/CeZrO_2$, while the propene

1016 conversion needs to be further improved to reach an efficiency comparable with the T_{50} of

1017 $Pd/CeZrO_2$. Further, very good results are obtained for the propane conversion, e.g.

1018 comparable with the efficiency achieved using the $Pd/CeZrO_2$ commercial catalyst. In terms of

1019 NO conversion, lower performances are recorded as compared to the PGM containing

1020 catalysts. However, this research demonstrates that the developed materials are very

1021 promising for the use in TWC application as noble metal free catalysts, compared to the

1022 classical catalysts composition. These new materials have proven to exhibit a considerably

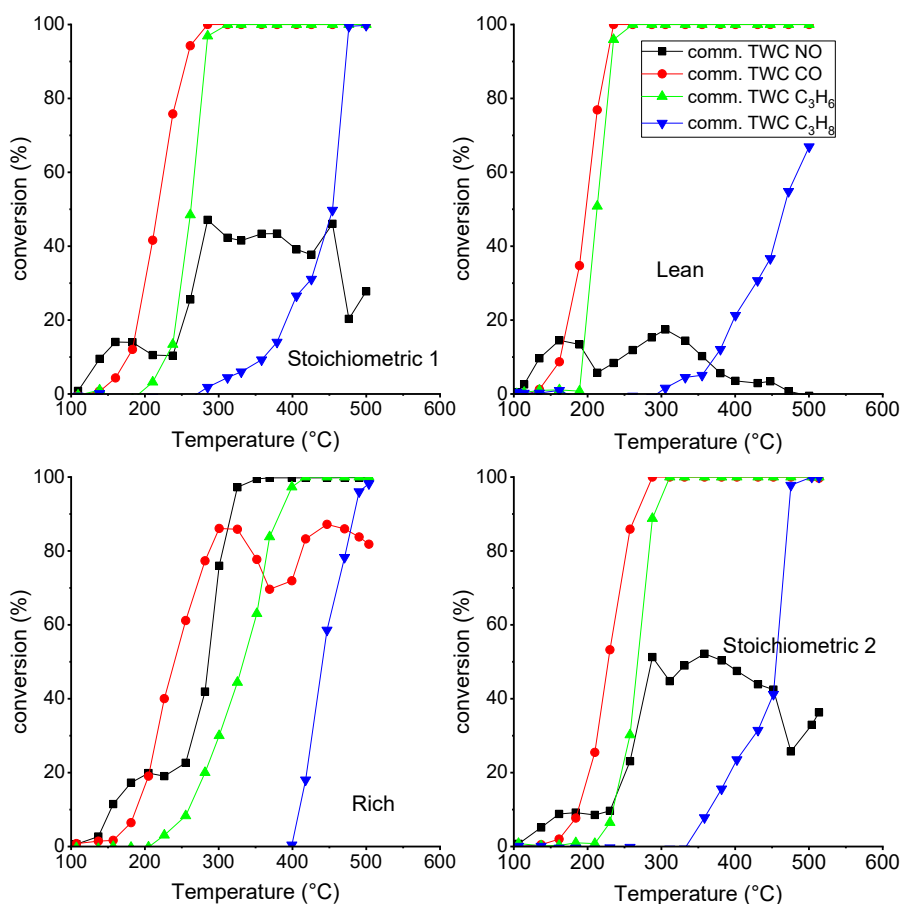1023 good performance for the oxidation of CO, propene and propane.

1024
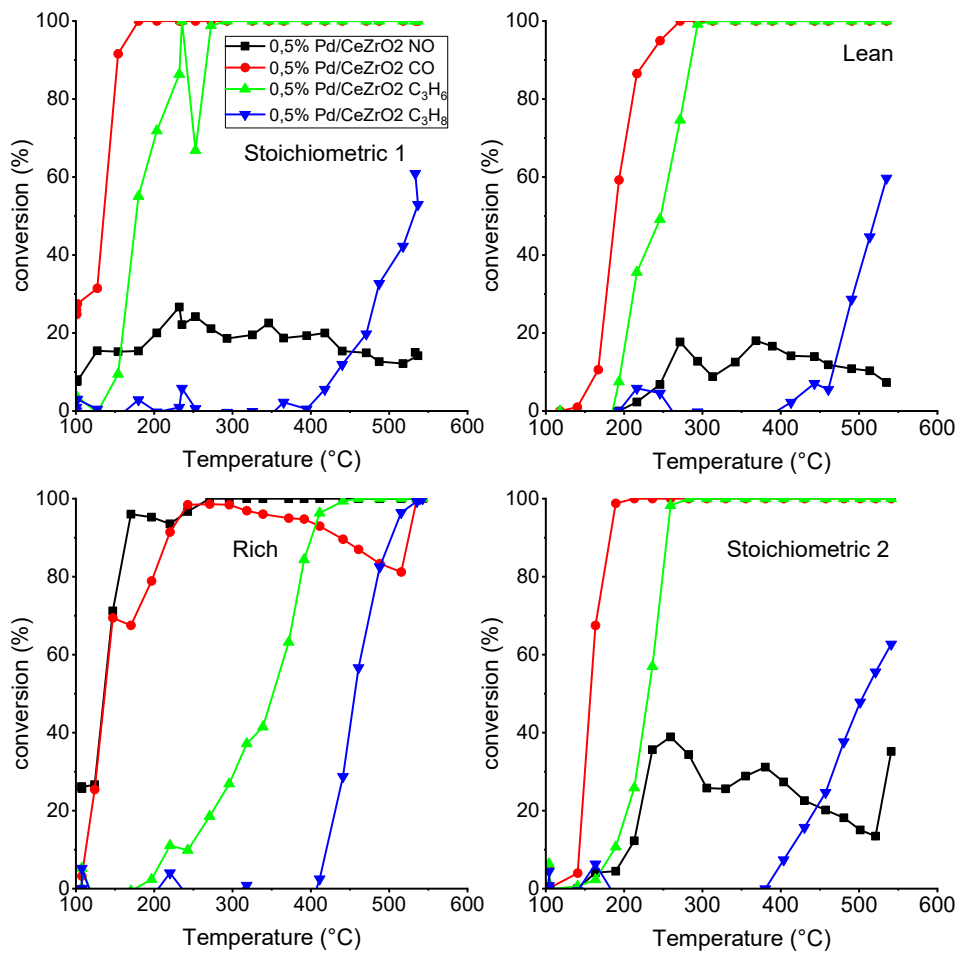
1025

Supplementary Figure 22: Conversion profiles for 0.5% Pd/CeZrO₂. Top left: first stoichiometric cycle, top right: lean cycle,

bottom left: rich cycle, bottom right: second stoichiometric cycle.

1028

Supplementary Figure 23: Conversion profiles for the commercial TWC catalyst. Top left: first stoichiometric cycle, top right:

lean cycle, bottom left: rich cycle, bottom right: second stoichiometric cycle.

Evaluation of the stability of the catalysts and structural investigation of the spent catalysts

In order to verify the stability of the catalysts after the catalytic tests, for the entire series, the XRD patterns were recorded for the used catalysts (Supplementary Figures 24 and 25). No structural modification was observed for the ZCA-600 and C/ZA-600 after the catalytic tests, as the XRD patterns are very comparable, while in the case of ZCAT-600 and C/ZAT-600, the presence of Cu_2O is noticed after the real conditions of the catalytic tests.

1039 Interestingly, the XRD patterns of MCAT-600 before and after the catalytic test associated with

1040 the spinel-like structure (initially $Cu_{1.5}Mn_{1.5}O_4$) are shifted. This shift is clearly noticed for the

1041 (115) and (044) planes at 57.6° and 63.3° (**¡Error! No se encuentra el origen de la**

1042 **referencia.**26). The newly formed structure is closer to $CuMn_2O_4$ (PDF 00-034-1400), while

1043 TiO_2 (rutile) and CuO crystal phases also appear now. For the other three manganese

1044 containing materials, a CuO phase is still not detected in the XRD patterns. Similar to the initial

1045 analysis, C/MZAT-600 consists again out of the mixed oxide phases of manganese ($CuMn_2O_4$

1046 and $ZnMn_2O_4$), while two new structures appear, namely rutile and a slightly different titanate

1047 phase, with an ilmenite ($FeTiO_3$, PDF 00-029-0733) structure. This ilmenite-like system is in

1048 this case likely a Zn-doped $MnTiO_3$ composition, for example $Mn_xZn_{1-x}TiO_3$. After the catalytic

1049 test, C/MA-600 patterns present features belonging only to Mn_3O_4, while Mn_2O_3 is no longer

1050 detected, as before the test. Contrary, the corresponding C/MT-600 consists outof similar

1051 components before and after the catalytic test (Mn_3O_4, Mn_2O_3, rutile).
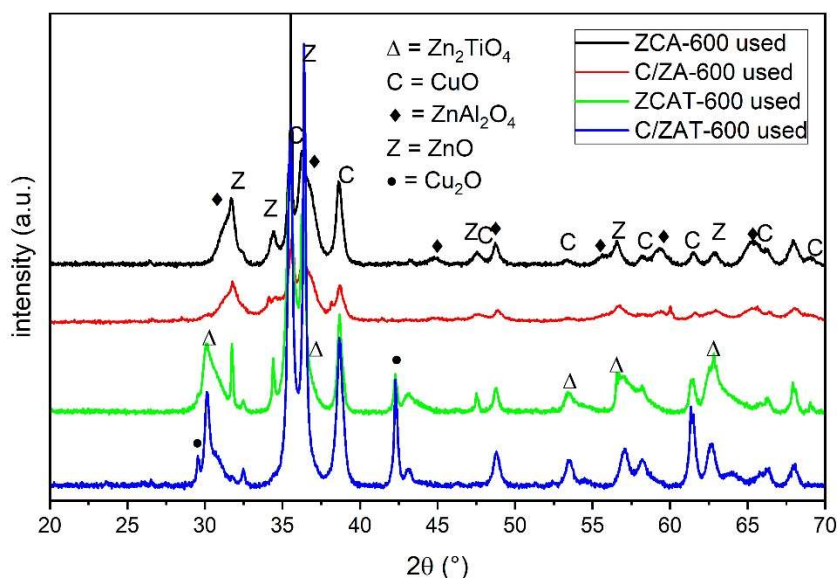
1052

1053 *Supplementary figure 24: XRD-patterns of ZCA-600, ZCAT-600, C/ZA-600 and C/ZAT-600 after the catalytic test.*
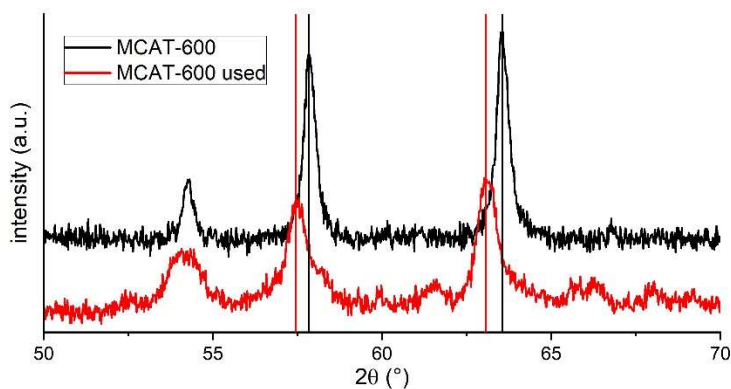
1054
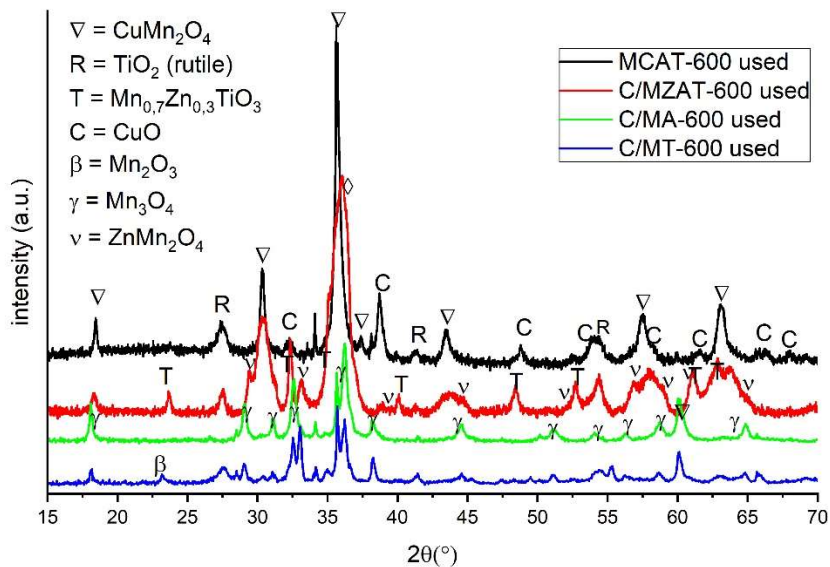
1055

1056   *Supplementary figure 25: XRD-patterns of MCAT-600, C/MZAT-600, C/MA-600 and C/MT-600 after the catalytic test.*

1057

1058

1059   *Supplementary figure 26: Detail of the XRD-patterns of MCAT-600 before and after the catalytic test.*

1060

1061

1062   References

1063   Mejía-Centeno, I., Castillo, S., Fuentes, G.A., 2012. Enhanced emissions of NH3, N2O and H2 from a

1064   Pd-only TWC and supported Pd model catalysts: Light-off and sulfur level studies. Appl. Catal. B

1065   Environ. 119–120, 234–240. https://doi.org/https://doi.org/10.1016/j.apcatb.2012.02.030

1066   Nevalainen, P., Kinnunen, N.M., Kirveslahti, A., Kallinen, K., Maunula, T., Keenan, M., Suvanto, M.,

1067   2018. Formation of NH3 and N2O in a modern natural gas three-way catalyst designed for

1068   heavy-duty vehicles: the effects of simulated exhaust gas composition and ageing. Appl. Catal. A

1069   Gen. 552, 30–37. https://doi.org/https://doi.org/10.1016/j.apcata.2017.12.017

1070 Schön, A., Dacquin, J.-P., Dujardin, C., Granger, P., 2017. Catalytic Activity and Thermal Stability of

1071   LaFe1−xCuxO3 and La2CuO4 Perovskite Solids in Three-Way-Catalysis. Top. Catal. 60, 300–306.

1072   https://doi.org/10.1007/s11244-016-0615-x

1073 Schön, A., Dacquin, J.-P., Granger, P., Dujardin, C., 2018. Non stoichiometric La1-yFeO3 perovskite-

1074   based catalysts as alternative to commercial three-way-catalysts? – Impact of Cu and Rh

1075   doping. Appl. Catal. B Environ. 223, 167–176.

1076   https://doi.org/https://doi.org/10.1016/j.apcatb.2017.06.026

1077 Schön, A., Dujardin, C., Dacquin, J.-P., Granger, P., 2015. Enhancing catalytic activity of perovskite-

1078   based catalysts in three-way catalysis by surface composition optimisation. Catal. Today 258,

1079   543–548. https://doi.org/https://doi.org/10.1016/j.cattod.2014.11.002

1080 Wu, J., Dacquin, J.P., Cordier, C., Dujardin, C., Granger, P., 2019. Optimization of the Composition of

1081   Perovskite Type Materials for Further Elaboration of Four-Way Catalysts for Gasoline Engine.

1082   Top. Catal. 62, 368–375. https://doi.org/10.1007/s11244-018-1083-2

1083 Wang, J., Chen, H., Hu, Z., Yao, M., Li, Y., 2015. A Review on the Pd-Based Three-Way Catalyst. Catal.

1084   Rev. 57, 79–144. https://doi.org/10.1080/01614940.2014.977059

1085 Yuan, D., Li, X., Zhao, Q., Zhao, J., Tadé, M., Liu, S., 2014. A novel CuTi-containing catalyst derived

1086   from hydrotalcite-like compounds for selective catalytic reduction of NO with C3H6 under lean-

1087   burn conditions. J. Catal. 309, 268–279. https://doi.org/10.1016/j.jcat.2013.09.010

1088